

This work was written as part of one of the author's official duties as an Employee of the United States Government and is therefore a work of the United States Government. In accordance with 17 U.S.C. 105, no copyright protection is available for such works under U.S. Law.

Public Domain Mark 1.0

<https://creativecommons.org/publicdomain/mark/1.0/>

Access to this work was provided by the University of Maryland, Baltimore County (UMBC) ScholarWorks@UMBC digital repository on the Maryland Shared Open Access (MD-SOAR) platform.

**Please provide feedback**

Please support the ScholarWorks@UMBC repository by emailing [scholarworks-group@umbc.edu](mailto:scholarworks-group@umbc.edu) and telling us what having access to this work means to you and why it's important to you. Thank you.



# Giant Outer Transiting Exoplanet Mass (GOT 'EM) Survey. III. Recovery and Confirmation of a Temperate, Mildly Eccentric, Single-transit Jupiter Orbiting TOI-2010

Christopher R. Mann<sup>1,2</sup> , Paul A. Dalba<sup>3,4,46</sup> , David Lafrenière<sup>1,2</sup> , Benjamin J. Fulton<sup>5,6</sup> , Guillaume Hébrard<sup>7,8</sup> , Isabelle Boisse<sup>9</sup> , Shweta Dalal<sup>7,10</sup> , Magali Deleuil<sup>9</sup> , Xavier Delfosse<sup>11</sup> , Olivier Demangeon<sup>12</sup> , Thierry Forveille<sup>13</sup> , Neda Heidari<sup>9</sup> , Flavien Kiefer<sup>14</sup> , Eder Martioli<sup>7,15</sup> , Claire Moutou<sup>16</sup> , Michael Endl<sup>17</sup> , William D. Cochran<sup>17</sup> , Phillip MacQueen<sup>18</sup> , Franck Marchis<sup>4,9</sup> , Diana Dragomir<sup>19</sup> , Arvind F. Gupta<sup>20,21</sup> , Dax L. Feliz<sup>22</sup> , Belinda A. Nicholson<sup>23,24</sup> , Carl Ziegler<sup>25</sup> , Steven Villanueva, Jr.<sup>26,27</sup> , Jason Rowe<sup>27</sup> , Geert Jan Talens<sup>2,28</sup> , Daniel Thorngren<sup>29</sup> , Daryll LaCourse<sup>30</sup> , Tom Jacobs<sup>31</sup> , Andrew W. Howard<sup>32</sup> , Allyson Bieryla<sup>33</sup> , David W. Latham<sup>33</sup> , Markus Rabus<sup>34</sup> , Tara Fetherolf<sup>35,48</sup> , Coel Hellier<sup>36</sup> , Steve B. Howell<sup>37</sup> , Peter Plavchan<sup>38</sup> , Michael Reefer<sup>38,39</sup> , Deven Combs<sup>38</sup> , Michael Bowen<sup>38</sup> , Justin Wittrock<sup>38</sup> , George R. Ricker<sup>40</sup> , S. Seager<sup>40,41,42</sup> , Joshua N. Winn<sup>28</sup> , Jon M. Jenkins<sup>37</sup> , Thomas Barclay<sup>43,44</sup> , David Watanabe<sup>45</sup> , Karen A. Collins<sup>33</sup> , Jason D. Eastman<sup>33</sup> , and Eric B. Ting<sup>37</sup>

<sup>1</sup> Département de Physique, Université de Montréal, Montréal, QC, Canada; [christopher.mann@umontreal.ca](mailto:christopher.mann@umontreal.ca)  
<sup>2</sup> Trotter Institute for Research on Exoplanets (iREx), Canada  
<sup>3</sup> Department of Astronomy and Astrophysics, University of California, Santa Cruz, CA 95064, USA  
<sup>4</sup> SETI Institute, Carl Sagan Center, 339 Bernardo Ave, Suite 200, Mountain View, CA 94043, USA  
<sup>5</sup> Cahill Center for Astronomy & Astrophysics, California Institute of Technology, Pasadena, CA 91125, USA  
<sup>6</sup> IPAC-NASA Exoplanet Science Institute, Pasadena, CA 91125, USA  
<sup>7</sup> Institut d'astrophysique de Paris, UMR7095 CNRS, Université Pierre & Marie Curie, 98bis boulevard Arago, 75014 Paris, France  
<sup>8</sup> Observatoire de Haute-Provence, CNRS, Université d'Aix-Marseille, 04870 Saint-Michel-l'Observatoire, France  
<sup>9</sup> Laboratoire d'Astrophysique de Marseille, Université de Provence, UMR6110 CNRS, 38 rue F. Joliot Curie, 13388 Marseille cedex 13, France  
<sup>10</sup> Department of Astrophysics, University of Exeter, Stocker Road, Exeter EX4 4QL, UK  
<sup>11</sup> Univ. Grenoble Alpes, CNRS, IPAG, 38000 Grenoble, France  
<sup>12</sup> Instituto de Astrofísica e Ciências do Espaço, Universidade do Porto, CAUP, Rua das Estrelas, 4150-762 Porto, Portugal  
<sup>13</sup> Université Grenoble Alpes, CNRS, IPAG, 38000 Grenoble, France  
<sup>14</sup> LESIA, Observatoire de Paris, Université PSL, CNRS, Sorbonne Université, Université de Paris, 5 place Jules Janssen, 92195 Meudon, France  
<sup>15</sup> Laboratório Nacional de Astrofísica, Rua Estados Unidos 154, 37504-364, Itajubá - MG, Brazil  
<sup>16</sup> Université de Toulouse, CNRS, IRAP, 14 avenue Belin, 31400 Toulouse, France  
<sup>17</sup> McDonald Observatory and Center for Planetary Systems Habitability, The University of Texas at Austin, Austin, TX 78730, USA  
<sup>18</sup> McDonald Observatory, The University of Texas at Austin, 2515 Speedway Boulevard, Stop C1400, Austin, TX 78712, USA  
<sup>19</sup> Department of Physics and Astronomy, University of New Mexico, 1919 Lomas Boulevard NE Albuquerque, NM, 87131, USA  
<sup>20</sup> Department of Astronomy & Astrophysics, 525 Davey Laboratory, The Pennsylvania State University, University Park, PA 16802, USA  
<sup>21</sup> Center for Exoplanets and Habitable Worlds, 525 Davey Laboratory, The Pennsylvania State University, University Park, PA 16802, USA  
<sup>22</sup> American Museum of Natural History, 200 Central Park West, Manhattan, NY 10024, USA  
<sup>23</sup> Centre for Astrophysics, University of Southern Queensland, Toowoomba, 4350, Australia  
<sup>24</sup> Sub-department of Astrophysics, University of Oxford, Keble Road, Oxford OX13RH, UK  
<sup>25</sup> Department of Physics, Engineering and Astronomy, Stephen F. Austin State University, 1936 North Street, Nacogdoches, TX 75962, USA  
<sup>26</sup> NASA Goddard Space Flight Center, Exoplanets and Stellar Astrophysics Laboratory (Code 667), Greenbelt, MD 20771, USA  
<sup>27</sup> Bishops University, 2600 College Street, Sherbrooke, QC J1M 1Z7, Canada  
<sup>28</sup> Department of Astrophysical Sciences, Princeton University, 4 Ivy Lane, Princeton, NJ 08544, USA  
<sup>29</sup> Department of Physics & Astronomy, Johns Hopkins University, Baltimore, MD 21210 USA  
<sup>30</sup> Amateur Astronomer, 7507 52nd Pl NE, Marysville, WA 98270, USA  
<sup>31</sup> Amateur Astronomer, 12812 SE 69th Place, Bellevue WA 98006, USA  
<sup>32</sup> Department of Astronomy, California Institute of Technology, Pasadena, CA 91125, USA  
<sup>33</sup> Center for Astrophysics | Harvard & Smithsonian, 60 Garden Street, Cambridge, MA 02138, USA  
<sup>34</sup> Departamento de Matemática y Física Aplicadas, Facultad de Ingeniería, Universidad Católica de la Santísima Concepción, Alonso de Rivera 2850, Concepción, Chile  
<sup>35</sup> Department of Earth and Planetary Sciences, University of California Riverside, 900 University Avenue, Riverside, CA 92521, USA  
<sup>36</sup> Astrophysics Group, Keele University, Staffordshire ST5 5BG, UK  
<sup>37</sup> NASA Ames Research Center, Moffett Field, CA 94035, USA  
<sup>38</sup> Department of Physics & Astronomy, George Mason University, 4400 University Drive MS 3F3, Fairfax, VA 22030, USA  
<sup>39</sup> Kavli Institute for Astrophysics and Space Research, Massachusetts Institute of Technology, 77 Massachusetts Avenue, Cambridge, MA 02139, USA  
<sup>40</sup> Department of Physics and Kavli Institute for Astrophysics and Space Research, Massachusetts Institute of Technology, Cambridge, MA 02139, USA  
<sup>41</sup> Department of Earth, Atmospheric and Planetary Sciences, Massachusetts Institute of Technology, Cambridge, MA 02139, USA  
<sup>42</sup> Department of Aeronautics and Astronautics, Massachusetts Institute of Technology, Cambridge, MA 02139, USA  
<sup>43</sup> NASA Goddard Space Flight Center, 8800 Greenbelt Road, Greenbelt, MD 20771, USA  
<sup>44</sup> University of Maryland, Baltimore County, 1000 Hilltop Circle, Baltimore, MD 21250, USA  
<sup>45</sup> Planetary Discoveries in Fredericksburg, VA 22405, USA

Received 2023 May 16; revised 2023 September 27; accepted 2023 September 28; published 2023 November 13



Original content from this work may be used under the terms of the [Creative Commons Attribution 4.0 licence](https://creativecommons.org/licenses/by/4.0/). Any further distribution of this work must maintain attribution to the author(s) and the title of the work, journal citation and DOI.

<sup>46</sup> Heising-Simons 51 Pegasi b Postdoctoral Fellow.

<sup>47</sup> NPP Fellow.

<sup>48</sup> UC Chancellor's Fellow.

## Abstract

Large-scale exoplanet surveys like the Transiting Exoplanet Survey Satellite (TESS) mission are powerful tools for discovering large numbers of exoplanet candidates. Single-transit events are commonplace within the resulting candidate list due to the unavoidable limitation of the observing baseline. These single-transit planets often remain unverified due to their unknown orbital periods and consequent difficulty in scheduling follow-up observations. In some cases, radial velocity (RV) follow up can constrain the period enough to enable a future targeted transit detection. We present the confirmation of one such planet: TOI-2010 b. Nearly three years of RV coverage determined the period to a level where a broad window search could be undertaken with the Near-Earth Object Surveillance Satellite, detecting an additional transit. An additional detection in a much later TESS sector solidified our final parameter estimation. We find TOI-2010 b to be a Jovian planet ( $M_P = 1.29 M_{\text{Jup}}$ ,  $R_P = 1.05 R_{\text{Jup}}$ ) on a mildly eccentric orbit ( $e = 0.21$ ) with a period of  $P = 141.83403$  days. Assuming a simple model with no albedo and perfect heat redistribution, the equilibrium temperature ranges from about 360 to 450 K from apastron to periastron. Its wide orbit and bright host star ( $V = 9.85$ ) make TOI-2010 b a valuable test bed for future low-insolation atmospheric analysis.

*Unified Astronomy Thesaurus concepts:* [Exoplanet astronomy \(486\)](#); [Exoplanet systems \(484\)](#); [Exoplanet dynamics \(490\)](#); [Exoplanet detection methods \(489\)](#)

## 1. Introduction

Following its launch in 2018, the Transiting Exoplanet Survey Satellite (TESS) mission (Ricker et al. 2015) has discovered many thousands of new exoplanet candidates. As per its mission mandate, most of these targets orbit stars bright enough for detailed follow-up characterization. While TESS’s nearly full-sky coverage and bright object target list are undeniably valuable qualities, they do come with drawbacks. One of the most notable is its limited temporal coverage of a given patch of sky. TESS’s observational strategy has been to shift its viewing angle every 25–30 days to a new sector. A portion of the sky experiences field overlap between sectors, but a large fraction ( $\sim 63\%$ ) receives only month-long baseline coverage. This is obviously detrimental for the detection of planets with orbital periods longer than  $\sim 30$  days. At best, TESS might catch one single transit in these regions before moving on to the next sector. Returning to the field in subsequent sectors can help, but does not guarantee another transit detection. Even catching a second transit detection typically leaves many possibilities for the orbital period depending on how many transits may have occurred during the unobserved time interval (Cooke et al. 2021). Without knowledge of the period, certain intrinsic system parameters remain unobtainable or strongly correlated. In particular, the semimajor axis and the period (both of which affect transit duration) are largely degenerate. As such, determination of stellar irradiation is unavailable. Attempted measurements of eccentricity and the argument of pericenter are also mostly uninformative. Lacking a clear picture of the orbital structure makes quantifying the system quite challenging. In addition, without strong constraints on the period via multiple transit detections or extensive radial velocity (RV) follow up, scheduling any sort of additional transit-based observations (e.g., transmission/emission spectroscopy, Rossiter–McLaughlin (RM) effect, etc.) becomes nearly impossible.

This is unfortunately the fate of most long-period single-transiting planet candidates in the TESS catalog. To date, more than 98% of the 6000+ TESS Objects of Interest (TOIs) with known periods are on orbits shorter than 50 days (Exoplanet Follow-up Observing Program; doi:10.26134/ExoFOP5), and many of those that have longer reported orbits are poorly characterized and require further verification. Even if a rough period estimate can be established with RV measurements, the

timing uncertainty of future transits grows with each subsequently unobserved transit ( $\sigma_{T_n} \propto n\sigma_P$ , where  $n$  is the number of transits since the period uncertainty,  $\sigma_P$ , was calculated). Generally, multiple transit observations are needed to provide tight constraints on the period and keep future timing uncertainties small.

Both transit and RV detection methods suffer observation and detection biases against long-period planets. In transit surveys, such planets require much longer baselines to capture sufficient events (Beatty & Gaudi 2008). With finite data sets, their folded multitransit signal-to-noise ratio (S/N) builds more slowly, making shallower transit events especially hard to detect. Their wide orbital geometries naturally lead to lower transit probabilities, reducing the number of expected events in a given search sample. RV measurements, which are complementary to transit observations, are also hindered by wider orbits. The signal amplitude shrinks and it takes longer to cover a full orbit.

Despite and because of these challenges, there is real value in improving our catalog of longer-period planets with their cooler equilibrium temperatures (Fortney et al. 2020). Due to these biases and accompanying investment required to study them, long-period planets tend to fall by the wayside and become underrepresented in exoplanet catalogs. Orbital periods of about 50 days mark a notable boundary in our confirmed planet databases. Given that every planet in our own solar system orbits with a period  $> 50$  days, the restriction to our known exoplanet population is quite staggering. By confirming and cataloging these wide-orbit planets we build up our understanding of the physical and orbital characteristics within this sparsely measured population.

Though they are few in number, our solar system giants provide detailed data on large cold planets, even allowing in situ measurements (e.g., the Galileo Entry Probe; Niemann et al. 1998). Hot, giant, transiting exoplanets also comprise a high-quality data set due to their large sample size and relative ease of detection. Temperate transiting planets in between these extremes require particular effort to observe due to their adverse observational biases. However, diligent confirmation studies can still accomplish precise measurements of radius, mass, and orbital structure. These studies provide information to understand the long-period planets as individuals, and as a population, better.

Another advantage of these cool giants is that they are more directly comparable to our well-studied cold solar system giants in that they do not exhibit the hot-Jupiter radius anomaly (Miller & Fortney 2011; Thorngren et al. 2016). The relative simplicity of modeling them acts as a valuable control group for understanding hot-Jupiter inflation. Though RV surveys have measured masses for many cool/cold ( $T_{\text{eq}} \lesssim 500$  K) planets, few of them exhibit transits and few of those have reasonably bright hosts, severely limiting their potential for atmospheric characterization. It is a challenge to create generalized chemical or structural atmospheric models that can span the broad temperature range of the giant planet population without having a solid testing ground in the intermediate range (Gao et al. 2021). Chasing down the longest-period targets in the TESS sample helps bridge this gap (e.g., Dalba et al. 2022). In terms of atmospheric chemistry, the cooler atmospheres may contain disequilibrium by-products that would serve as valuable probes of atmospheric physics (Fortney et al. 2020). Spectroscopic endeavors can use these lower-insolation targets to tease apart the composition transition between the very cold and very hot giant planet atmospheres.

Stellar insolation can also have many complex effects on a planet’s atmosphere. The question of X-ray and ultraviolet (XUV)-driven mass loss frequently arises in the context of the super-Earth and sub-Neptune populations (Owen & Wu 2013; Dong et al. 2017; Mordasini 2020). Irradiation levels are also important for general structure and evolution models as well as atmospheric circulation and photochemistry in cool planets (Hörsst et al. 2018). Insolation ought to push the radiative–convective boundary deeper, but also seems to drive the radius anomaly which pushes the boundary back up along with the planet radius (Thorngren et al. 2019). Given the inverse-square law of stellar irradiation, wider-orbit planets will be significantly less affected by XUV-driven mass loss, preserving more of their primordial composition. Building a sample of planets with reduced insolation will help with the creation of more broadly applicable planetary models.

Long-period planets also provide test cases for system dynamics. Models describing the formation and migration processes thought to be responsible for the hot-Jupiter population are generally of two categories: protoplanetary disk torques (Goldreich & Tremaine 1980; Lin & Papaloizou 1986; Ward 1997; Baruteau et al. 2014) or high-eccentricity migration (Rasio & Ford 1996; Wu & Murray 2003; Nagasawa et al. 2008; Wu & Lithwick 2011). With the end products often being very similar, knowledge of intermediate-separation transiting planets, their companions, and their environments will help distinguish between these types of models. Transit and RV surveys are always biased against long-period planets, so filling out the eccentricity distribution of long-period giants still requires additional effort (e.g., Dalba et al. 2021). Obliquity measurements (using either the RM effect or Doppler tomography) have also been done almost exclusively on short-period giants thus far.

TOI-2010 (details in Table 1) was flagged as containing a transiting planet candidate after a single transit was detected on 2019 August 16. The transiting body, designated TOI-2010.01, did not exhibit a retransit in the remainder of TESS’s primary mission. In this manuscript we confirm and characterize its planetary nature, and so we will hereafter refer to it by the designation TOI-2010 b in accordance with standard planetary nomenclature. Its initial single-transit status inspired an intensive

**Table 1**  
Host Star Information

Parameter	Value	Source
TESS ID	TOI-2010	[1]
TIC ID	TIC 26547036	[1]
Gaia ID	2136815881249993600	[2]
$\alpha$	19 <sup>h</sup> 28 <sup>m</sup> 40 <sup>s</sup> .07	[2]
$\delta$	+53 <sup>d</sup> 29 <sup>m</sup> 14 <sup>s</sup> .53	[2]
$m_B$	10.48	[3]
$m_V$	9.85	[3]
$m_G$	9.70	[2]
$m_I$	8.66	[4]
$m_H$	8.34	[4]
$m_K$	8.28	[4]
Spectral type	F0	[5]
Parallax [mas]	9.2219 ± 0.0107	[2]

**Note.**

- [1] ExoFOP; doi:[10.26134/ExoFOP5](https://doi.org/10.26134/ExoFOP5).
- [2] Gaia Collaboration (2020).
- [3] Høg et al. (2000).
- [4] Cutri et al. (2003).
- [5] Simbad; doi:[10.17616/R39W29](https://doi.org/10.17616/R39W29).

RV campaign which constrained the period well enough to make feasible a photometric search for a second transit. While both of these efforts were successful, a much later TESS sector fortuitously revealed an additional transit during the late stages of this manuscript preparation, confirming our findings and providing even tighter parameter determination.

We present the various data and observations that contributed to this planet confirmation in Section 2. We then describe the various analyses carried out to characterize the star, planet, and system as a whole in Section 3. Sections 4 and 5 contain descriptions and discussion of our findings, respectively. Finally, a brief summary of the entire study is presented in Section 6.

## 2. Data and Observations

Numerous observations of this planet candidate were made by the TESS Follow-up Observing Program (TFOP). Some of them are overlapping in their coverage or scope, and many were intermediate steps of target validation used to green-light more intensive observations. We list all the contributions in the subsections below for completeness and recognition, but note that not every data set is included in the analysis that follows.

### 2.1. Discovery and Sky-Monitoring Photometry

#### 2.1.1. TESS

In the early stages of the preparation of this manuscript, TOI-2010 had been observed at 2 minute cadence for Sectors 14, 15, 16, and 40 and the image data were reduced and analyzed by the Science Processing Operations Center (SPOC; Jenkins et al. 2016) at NASA Ames Research Center. A single transit was detected at the beginning of Sector 15 using an adaptive, wavelet-based matched filter (Jenkins 2002; Jenkins et al. 2010, 2020) on 2019 September 21. The signal was also independently discovered by the Visual Survey Group (Kristiansen et al. 2022) around the same time and forwarded to the attention of the TESS Single Transit Planet Candidate (TSTPC) working group for follow up. It was alerted by the



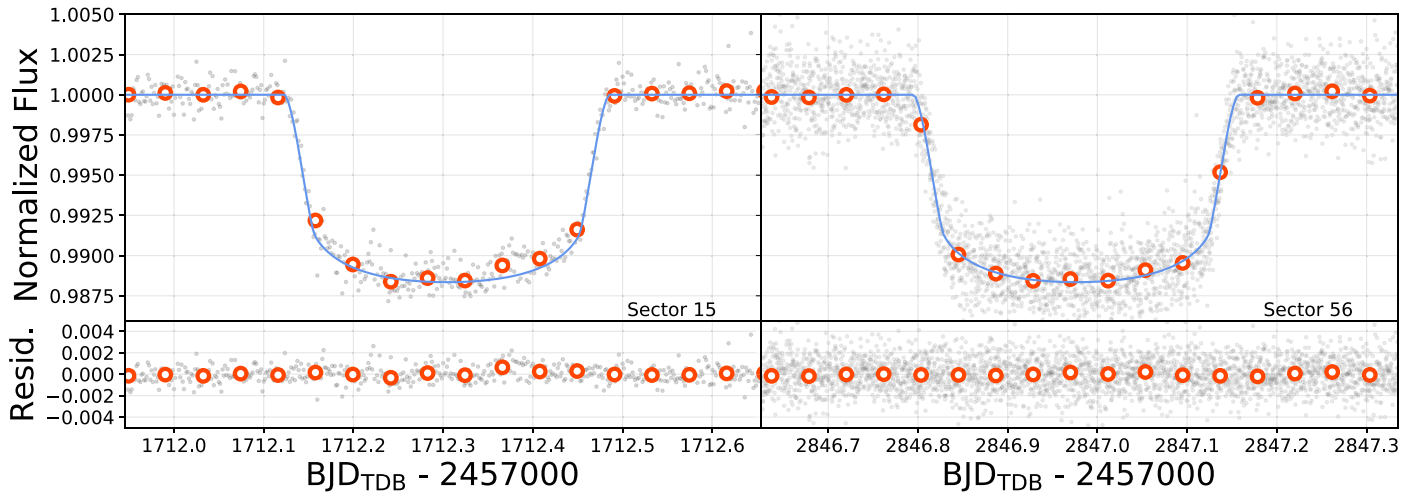


**Figure 1.** PDCSAP data of the TESS transit detection in Sector 15 (left) and Sector 56 (right). Sector 15 was imaged with a 120 s cadence, while Sector 56 included a 20 s cadence. All bins are 60 minutes.

TESS Science Office as a Community TOI (CTOI) on 2020 June 17. This single-transit event, though unambiguous due to its high S/N, posed a validation challenge due to its lack of period constraint.

During the late stages of manuscript preparation, TESS reobserved TOI-2010 in Sectors 54, 55, and 56 as part of its extended missions. An additional transit was detected in the Sector 56 light curve and included in our final analysis. A search by the SPOC of Sectors 14–56 reported a difference image centroiding result (Twicken et al. 2018) constraining the host star location to within  $2''.54 \pm 2''.9$  of the difference image centroid. This is in agreement with the low contamination by reported nearby Gaia stars.

We acquired the Pre-search Data Conditioning Simple Aperture Photometry (PDCSAP; Smith et al. 2012; Stumpe et al. 2012, 2014) flux data from the Milkuski Archive for Space Telescopes (MAST) for the 2 minute Sector 14, 15, 16, and 40 data (doi:10.17909/t9-nmc8-f686) and the 20 s Sector 54, 55, and 56 data (doi:10.17909/t9st5g-3177).

Before applying any light-curve fitting, we use the `lightcurve` (Lightcurve Collaboration et al. 2018) software package’s built-in `flatten` routine to remove any remaining PDCSAP variability. This applies a Savitzky–Golay filter (Savitzky & Golay 1964) to the light curves, fitting a low-order polynomial to a rolling subset of the data to remove low-frequency trends. The transit regions were masked during this process and the subset windows were chosen to be longer than the transit duration. We apply the same `flatten` routine to the 20 s cadence Sector 56 TESS data, applying an additional rolling sigma-clipping routine ( $3\sigma$  from the median in a window of  $\pm 100$  minutes) to remove outliers. The portions of the flattened light curve containing the transits and used for analysis are shown in Figure 1.

With the current Year 5 plan for the TESS mission, there are no scheduled visits to this region of the sky after Sector 56.

### 2.1.2. WASP

The field containing TOI-2010 was observed by the Wide Angle Search for Planets (WASP) transit-search survey (Pollacco et al. 2006) from 2008 to 2010. In each year the observing season spanned  $\sim 130$  nights, with the SuperWASP-North camera array observing the field on clear nights with a

typical 15 minute cadence. A total of 32,000 photometric data points were obtained using 200 mm,  $f/1.8$  Canon lenses backed by  $2k \times 2k$  CCDs. TOI-2010 is the only bright star in the  $48''$  extraction aperture.

The WASP data are dominated by systematics and red noise. While the transit depth is likely sufficient to show up in the WASP light curves, the survey mission relies on multiple repeated events to distinguish transits from noise. As a single-transit target at the time, WASP did not detect any events on the target. Even with the benefit of hindsight and a firm orbital ephemeris, the WASP coverage only overlaps with one predicted transit. The 4 hr span of data lies in the middle of a 8.7 hr transit, and the light curve shows no convincing transit-like features.

## 2.2. Candidate Vetting

Once established as a TOI, a number of vetting observations were undertaken. They were used to search for false positive indications, and to assess the target’s suitability for further follow-up observations.

### 2.2.1. Keck/HIRES Spectra

We obtained a spectrum of TOI-2010 with the High Resolution Echelle Spectrometer (HIRES; Vogt et al. 1994) on the Keck I telescope at W. M. Keck Observatory to explore false positive explanations for the single-transit event, to assess the quality of the host as a target for Doppler spectroscopy, and to conduct a basic spectral characterization of the host. Initial processing of the spectrum with `SpecMatch-Emp` (“Emp” indicating the “Empirical” flavor of the code; Yee et al. 2017) determined the stellar parameters. The results, along with the star’s bright magnitude indicated that it would likely be a suitable target for Doppler spectroscopy.

This Keck/HIRES measurement was taken under excellent seeing conditions and produced a spectrum with  $S/N \sim 200$ . Given this data quality it was used as the template spectrum with which the Levy RV measurements were extracted (see Section 2.3). Similarly, we favor the Keck/HIRES extracted stellar parameters over those from LCOGT/NRES and FLWO/TRES (Sections 2.2.2 and 2.2.3) due to the quality of the spectrum, though we note the close agreement of most

**Table 2**

Stellar Parameters from Independent Spectral Instruments/Measurements

Parameter	HIRES	NRES	TRES	Units
$T_{\text{eff}}$	$5917 \pm 75$	$5860 \pm 100$	$5795 \pm 50$	K
$\log g$	$4.412^{+0.023}_{-0.026}$	$4.5 \pm 0.1$	$4.42 \pm 0.10$	
[Fe/H]	$0.169^{+0.055}_{-0.056}$	$0.23 \pm 0.06$	$0.22 \pm 0.08$	
$M_*$	$1.107^{+0.050}_{-0.057}$	$1.139 \pm 0.049$	...	$M_{\odot}$
$R_*$	$1.084^{+0.028}_{-0.027}$	$1.106 \pm 0.074$	...	$R_{\odot}$
$v \sin i_*$	$<2.3$	$<4.4$	$<4.8$	$\text{km s}^{-1}$

**Note.**  $v \sin i_*$  values become challenging to constrain when at the few kilometers per second level as many line-broadening mechanisms are simultaneously at play on this scale (e.g., macroturbulence). We therefore treat the spectral estimates as upper limits.

parameters. Table 2 provides a comparison of these stellar parameters.

### 2.2.2. LCOGT/NRES Spectra

We scheduled spectroscopic observations for TOI-2010 on the Las Cumbres Observatory Global Telescope (LCOGT; Brown et al. 2013) Network of Robotic Echelle Spectrographs (NRES; Siverd et al. 2018). NRES comprises four identical echelle spectrographs in different observatories, covering a range of longitudes in the Northern and Southern Hemispheres. The resolving power of the echelle spectrographs is  $R \sim 53,000$ , covering the wavelength range 3900–8600 Å. We obtained four good-quality ( $S/N = 18$ –56) spectra with the NRES unit at the Wise Observatory between 2020 June 19 and 28. We used the BANZAI–NRES pipeline (McCully et al. 2022) to reduce the spectra and extract RVs, and the SpecMatch–Synthetic code for the stellar parameterization (Petigura 2015; Petigura et al. 2017).

While the NRES observations provided helpful early vetting of the system, we have chosen to exclude the four RV measurements from the analysis due to their much lower precision ( $>20 \text{ m s}^{-1}$ ). The derived stellar parameters are generally in close agreement with the Keck/HIRES values (Table 2).

### 2.2.3. FLWO/TRES Spectra

Three reconnaissance spectra of TOI-2010 were obtained on 2020 July 9, 18, and 27 with the Tillinghast Reflector Echelle Spectrograph (TRES; Fűrész 2008). TRES is an optical (390–910 nm) spectrograph with a resolving power of  $R \sim 44,000$  mounted on the 1.5 m Tillinghast Reflector telescope at the Fred Lawrence Whipple Observatory (FLWO). The spectra, with  $S/N$ s in the range of 25–35, were extracted using the TRES standard pipeline (Buchhave et al. 2010) and the stellar parameters were derived using the Stellar Parameter Classification (SPC; Buchhave et al. 2012, 2014) tool. SPC cross correlates the observed spectra against a grid of synthetic spectra based on Kurucz atmosphere models (Kurucz 1992), deriving the stellar effective temperature, surface gravity, metallicity, and rotational velocity.

In the same sense as the NRES spectra described above, these data were useful in the early classification of the star and ruling out of false positives, enabling more detailed measurements to be carried out. The FLWO/TRES stellar parameters are also generally in close agreement with the Keck/HIRES analysis (Table 2).

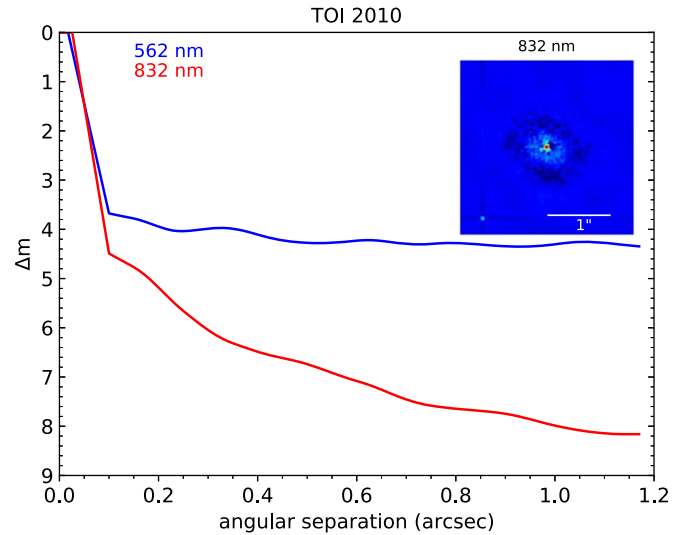


**Figure 2.** Contrast curves from Gemini-N/Alopeke speckle image. Curves show the  $5\sigma$  contrast limit. The faint source in the lower left of the inset image is a previously unresolved neighbor star not present in the Gaia DR3 catalog.

### 2.2.4. Gemini-N/Alopeke Imaging

Using the ‘Alopeke instrument mounted on the Gemini-North telescope we acquired high-contrast imaging of TOI-2010 on 2020 June 7 (Program ID: GN-2020A-Q-132). This observation was a part of the exoplanet follow-up campaign by Howell et al. (2021). With ‘Alopeke’s design, it can simultaneously capture imagery at both 562 and 832 nm. The resulting images were processed using the pipeline of Howell et al. (2011), and the resulting contrast curves are shown in Figure 2. Due to the clearly superior performance of the 832 nm filter, we use the red contrast curve for all analyses (e.g., Section 3.7).

One previously unknown nearby source was detected, seen in the lower left corner of the Figure 2 inset. This object is separated by  $1''.5$  at a position angle of  $138^\circ$  east of north. The brightness uncertainty on this neighbor is somewhat elevated as it lies outside the speckle correlation radius of  $\sim 1''.2$ . Speckle decorrelation begins to set in beyond this separation when the rays do not pass through the same atmospheric path. Our photometric estimate of the source places it at a  $\Delta \text{mag} = 5 \pm 0.5$ .

This source is not to be confused with the neighboring Gaia star discussed further in Section 4. The Gaia source lies at a separation of  $1''.9$  and a position angle of  $33^\circ$  east of north, beyond the field of view of our ‘Alopeke image. The  $1''.5$  source found in our ‘Alopeke image does not appear in Gaia’s DR2 or DR3 catalogs.

## 2.3. RVs

The reconnaissance spectra from Keck/HIRES, LCOGT/NRES, and FLWO/TRES were able to place sufficient constraints on the stellar parameters to identify TOI-2010 as a suitable candidate for precise RV measurements. We collected a total of 110 RV measurements (Figure 3, values in the Appendix) to make up our combined RV data set. These measurements come from three separate instruments, span 992 days, and uniformly sample the phase space of the 142 day periodic signal that stands out in the data.

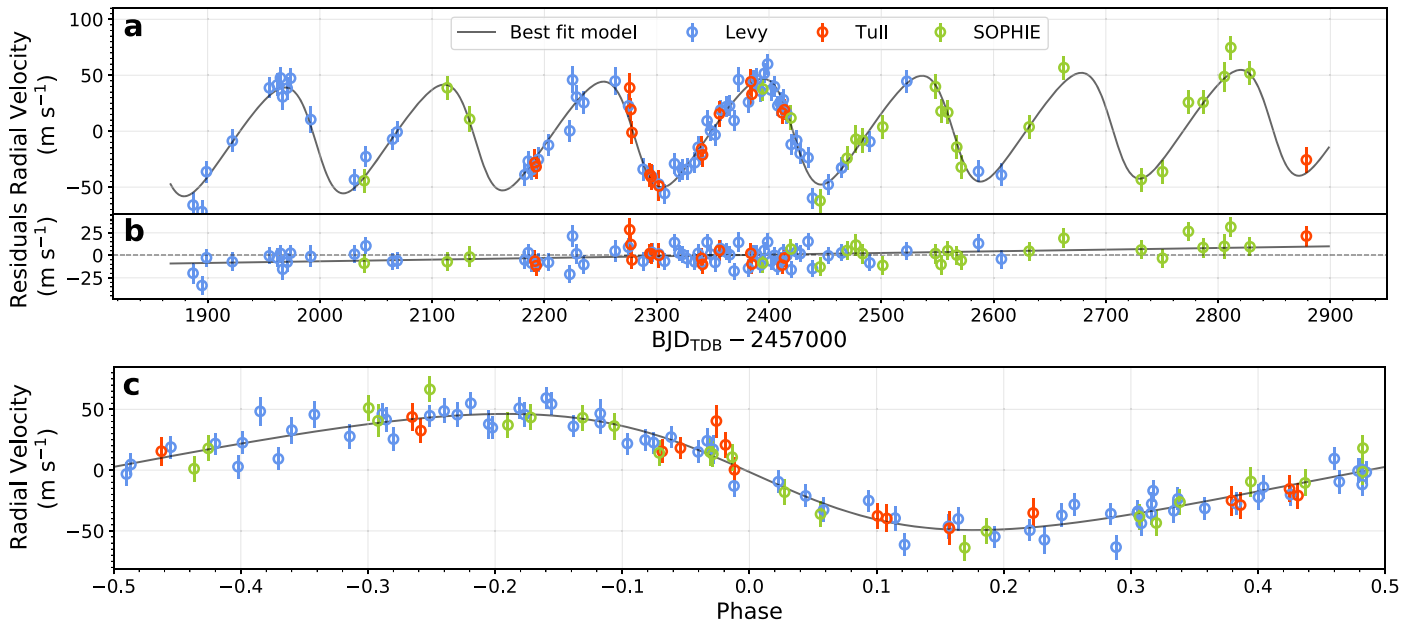


**Figure 3.** RV coverage of 110 measurements spanning  $\sim 2.7$  yr uniformly samples the full phase of the planet’s orbit. A small residual acceleration remains after the removal of the planet’s Keplerian signal.

### 2.3.1. Levy

In 2020 February (BJD = 2,458,887), we began to gather spectra of the target for RV measurements. We started with the Levy spectrograph installed on the 2.4 m Automated Planet Finder (APF) telescope at Lick Observatory in California, acquiring 70 spectra over a 2 yr period, carried out by the dynamic queue scheduler (Burt et al. 2015). The Levy spectrograph is a high-resolution ( $R \sim 114,000$ ) slit-fed optical echelle spectrometer (Radovan et al. 2010) that has previously been used to refine the orbital period and mass of single-transit planet candidates identified by TESS (e.g., Dalba et al. 2022). We gathered spectra with exposure times of 20–25 minutes (mostly 25), achieving S/N values of 50–100 at around 550 nm. An iodine cell in the light path allows for wavelength calibration and forward modeling of the stellar RV for each spectrum (Butler et al. 1996; Fulton et al. 2015). This forward modeling process relies on having a high-S/N spectrum that is used as a template. The HIRES spectrum described in Section 2.2.1, which had an S/N of roughly 200, was used to create this template spectrum for the extraction of the Levy RVs which were obtained with uncertainties of 4–7  $\text{m s}^{-1}$ .

We look for correlations in the  $\log R'_{\text{HK}}$  activity index (computed from the S-index using `PyAstronomy` routines) with RVs to determine if stellar activity may be biasing the measurements. We determine a correlation coefficient of  $0.10 \pm 0.05$  and a  $p$ -value of  $0.43 \pm 0.23$ , indicating no evidence of correlation.

### 2.3.2. Tull

We also gathered high-precision RV observations at the McDonald Observatory using the Tull coude spectrometer 2 (TS2) on the 2.7 m Harlan J. Smith Telescope (Tull et al. 1995). This cross-dispersed echelle white-pupil spectrometer was used in its “TS23” mode (indicating third focus) with an entrance slit of  $1''.2 \times 8''.2$ , giving a spectral resolving power of  $R = 60,000$  over most of the visible spectrum. A temperature-stabilized  $I_2$  gas absorption cell in front of the spectrograph entrance aperture

provided the velocity calibration. An exposure meter recorded the time series of flux entering the spectrograph, enabling us to compute the flux-weighted barycentric correction. A wave front sensor was used for telescope focus to optimize pupil illumination stability and throughput. We obtained the measurements with 20–30 minutes exposures, achieving an S/N per pixel of 62–96 (mean  $\sim 75$ ). The spectra are recorded on a  $2048 \times 2048$  pixel Tektronix CCD. All spectra were reduced and 1D spectra were extracted using standard IRAF routines (Tody 1986, 1993). In all, a total of 16 spectra of TOI-2010 were obtained between 2020 December 8 and 2022 October 26. RVs were computed using the AUSTRAL code (Endl et al. 2000), resulting in uncertainties of 9–12  $\text{m s}^{-1}$ .

We conduct a similar activity–RV correlation search as was done with the Levy, resulting in a coefficient of  $0.02 \pm 0.20$  and a  $p$ -value of  $0.59 \pm 0.26$  for Tull. Again, there is no indication of RV correlation.

### 2.3.3. SOPHIE

We started observing TOI-2010 with the Spectrographe pour l’Observation des Phénomènes des Intérieurs stellaires et des Exoplanètes (SOPHIE) in 2020 July, securing 25 spectroscopic measurements up to 2022 September. SOPHIE is a stabilized échelle spectrograph dedicated to high-precision RV measurements in optical wavelengths on the 193 cm Telescope at the Observatoire de Haute-Provence, France (Perruchot et al. 2008; Bouchy et al. 2009). We used the SOPHIE high-resolution mode (resolving power  $R = 75,000$ ). Depending on the weather conditions, the exposure times ranged from 11 to 30 minutes (typically 18 minutes) and their S/N per pixel at 550 nm ranged from 24 to 55 (typically 46). The corresponding RVs were extracted with the standard SOPHIE pipeline using cross-correlation functions (Bouchy et al. 2009) and including CCD charge transfer inefficiency correction (Bouchy et al. 2013). Following the method described, e.g., in Pollacco et al. (2008) and Hébrard et al. (2008), we estimated and corrected for the moonlight contamination using the second SOPHIE fiber aperture, which is targeted on the sky while the first



aperture points toward the star. We estimated that four of the 25 spectra were significantly polluted by moonlight; one of which was too contaminated and was excluded. The other three contaminated measurements were corrected, with corrections below  $20 \text{ m s}^{-1}$ . Thus our final SOPHIE data set included 24 measurements showing RV uncertainties ranging  $3\text{--}9 \text{ m s}^{-1}$ .

SOPHIE  $\log R'_{\text{HK}}$  activity measures similarly show no correlation with RV values. We determine a correlation coefficient of  $0.22 \pm 0.14$  and a  $p$ -value of  $0.38 \pm 0.27$ .

#### 2.4. Follow-up Photometry

The collective RV campaign was able to map out a clear planetary signal, but the period uncertainty was only constrained to the order of a few days. This was insufficient for reliable scheduling of transit observations, so we undertook a few efforts to catch a subsequent transit and fine-tune the period.

##### 2.4.1. GMU

We observed TOI-2010 with the George Mason University Observatory's 0.8 m Ritchey–Chretien telescope on the nights of the 2021 July 21 and 22 to capture a second transit. We imaged in  $R$  with an SBIG-16803 CCD with exposure times of 30 s repeated for a duration of  $\sim 5$  and 2.5 hr each night, respectively. Both nights were impacted by intermittent clouds, and single measurement precisions of 6.5 and 7.5 ppt were obtained per 30 s exposure. Data was reduced and plate-solved using a custom python code `alnitak`<sup>49</sup> and aperture photometry, reference star selection, and systematic detrending were performed with `AstroImageJ` (Collins et al. 2017).

This attempt was prompted due to a predicted transit (from preliminary RV fits) occurring very near the end of TESS Sector 40, and motivated by an absence of TESS coverage in Sector 41. Unfortunately, no transit was detected on either night. Given the broad transit timing uncertainty at the time, the narrow available observing windows, and the very long transit duration, the odds of detecting the transit here were quite low. Unbeknownst at the time, the transit occurred 1.8 days after the second observation. These data provided initial constraining power for refining the RV period, but do not benefit the global orbital model. As such, they are not included in the modeling of Section 3.

##### 2.4.2. NEOSSat

The Near-Earth Object Surveillance Satellite (NEOSSat) is a small spacecraft operated jointly by the Canadian Space Agency (CSA) and Defence Research and Development Canada (DRDC). It has a 15 cm telescope aperture and is capable of precision relative photometry (Abbasi et al. 2019). NEOSSat's clear-filter effective bandpass is approximately 400–900 nm.

As the RV data accumulated, preliminary joint fits (see Section 3 for details) of the RVs and TESS Sector 15 transit revealed a roughly 142 day period, albeit with broad uncertainties. The extended transit duration ( $\sim 8.7$  hr), wide timing uncertainty (on the order of a week), and long period made observing a subsequent transit from the ground extremely challenging. While NEOSSat had previously proven its capability with short-period exoplanet follow up (e.g., Fox &

Wiegert 2022), TOI-2010 b marked the first attempt at using the instrument to recover a long and uncertain period. With its space-based vantage point, NEOSSat has the capability to stare continuously at a target for an extended duration, interrupted only by Earth eclipse events and technical satellite operations. In mid-December of 2021 we employed NEOSSat to observe a  $\sim 6$  day ( $2\sigma$ ) window around the predicted transit. The telescope imaged TOI-2010 as continuously as was feasible during this time.

We reduced the raw images and extracted aperture photometry using a custom python pipeline developed for NEOSSat, available on GitHub.<sup>50</sup> With photometry in hand, we applied a principal component analysis (PCA) procedure to the raw photometry using other in-frame stars as reference to calculate a normalized relative flux light curve of the target. The PCA process removes time-varying trends in the photometry that are common across many stars in the frame. At this point there remained some residual variability for which the PCA could not account. This low-frequency variability was removed using a spline fit (discussed in Section 3.3). Even against this variability the deep transit event was clearly visible roughly 15 hr after the RV-predicted midpoint (well within the 3 day,  $1\sigma$  timing uncertainty).

This detection by NEOSSat provided the first precise period measurement for TOI-2010 b, and prompted the preparation of this manuscript. The much later transit detected in TESS's Sector 56 data agrees completely with the refined period. The NEOSSat light curve is displayed in Figure 4.

### 3. Analysis

As the RV campaign progressed, we made preliminary fits using the TESS light curve and the available RV data to place initial constraints on the orbital period. This allowed us refine the ephemeris enough to plan our follow-up search for a subsequent transit event. Once they became available, the additional transit detections (NEOSSat and TESS Sector 56) allowed for much more precise period determination.

For our final global fit, we use the IDL software package `EXOFASTv2` (Eastman et al. 2019). `EXOFASTv2` provides an integrated framework to analyze multiple exoplanet data sets jointly. Drawing from the IDL astronomy library (Landsman 1993), it simultaneously fits for wide ranges of stellar, planetary, orbital, and instrumental parameters in a self-consistent manner that leverages the rich complementarity of modern data sets.

The details listed below in Sections 3.1–3.3 pertain to the final fit, including archival spectral energy distribution (SED) measurements; RVs from Levy, Tull, and SOPHIE; and light curves from the initial TESS Sector 15 transit, the subsequent NEOSSat detection, and also the much later Sector 56 detection by TESS. The parameter posterior results are listed in Table 3. The fits converged fully by two different statistics: the Gelman–Rubin statistic,  $R_z$ , and the number of independent samples,  $T_z$ . We set very stringent thresholds of  $R_z < 1.01$  and  $T_z > 1000$ . We provide a brief description of the steps involved, but for precise details on the internal operations of `EXOFASTv2` please consult the primary paper by Eastman et al. (2019).

Beyond `EXOFASTv2`, we conduct several other independent analyses. We model the bulk metallicity of planet b with a

<sup>49</sup> <https://github.com/oalfaro2/alnitak>

<sup>50</sup> <https://github.com/jasonfrowe/neossat>



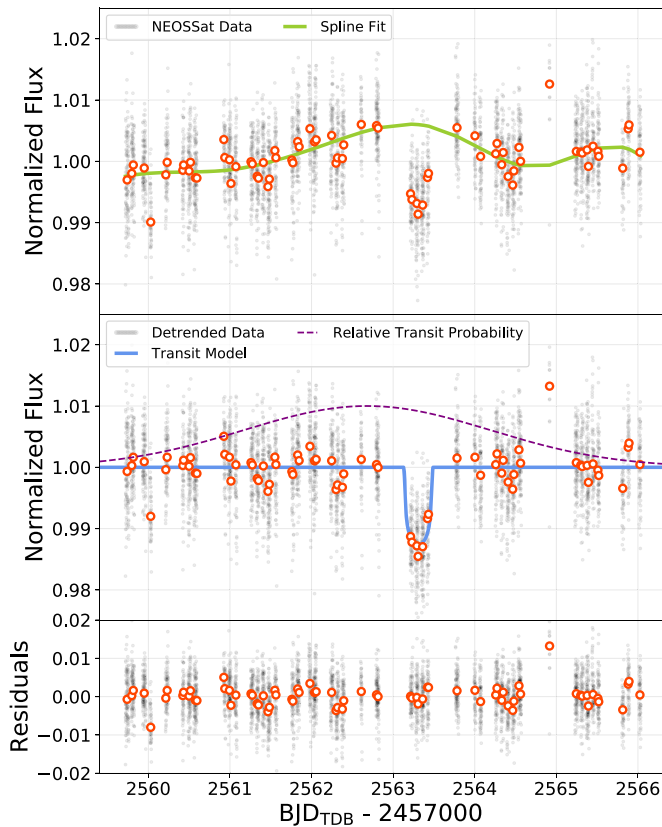


**Figure 4.** A week-long observation by NEOSSat. Gaps in the light curve are due to Earth eclipse and other necessary telescope operations. The star was imaged with a cadence of 23 s while on target. Displayed bins are 60 minutes. Top: a `KEPLERSPLINE` fit to the out-of-transit region to model systematics (discussed in Section 3.3). Middle: the transit fitted to the corrected light curve. The dashed purple curve shows relative probability of the expected transit based on the RV-derived period constraints available at the time of observation. Bottom: residuals of the transit fit.

custom software, and we analyze the photometric modulation of TOI-2010 to assess the stellar rotation. In discovering a slight acceleration across the RV measurements, we also conduct a search of mass–orbit parameter space to determine what type of additional companion could be the cause.

### 3.1. EXOFASTv2: SED/MIST Stellar Modeling

EXOFASTv2 fetches archival photometry from Galaxy Evolution Explorer (GALEX; Bianchi et al. 2011), Tycho-2 (Høg et al. 2000), UCAC4 (Zacharias et al. 2012), APASS (Henden et al. 2016), the Two Micron All Sky Survey (2MASS; Cutri et al. 2003), the Wide-field Infrared Survey Explorer (WISE; Cutri et al. 2021), Gaia (Gaia Collaboration et al. 2016), the Kepler INT Survey (Greiss et al. 2012), the UVB Photoelectric Catalog (Mermilliod 1994), and the Stroemgren–Crawford  $uvby\beta$  photometry catalog (Paunzen 2015), as well as extinctions from Schlegel et al. (1998) and Schlafly & Finkbeiner (2011) and parallaxes from Gaia DR2 (Gaia Collaboration et al. 2018). Allowing photometric uncertainties to be inflated in case of underestimation, it then fits an SED model to this archival photometry using the parallax value and a library of stellar atmospheres. The stellar physics are constrained from either the empirical relations laid out by Torres et al. (2010), the Yonsei Yale stellar evolutionary models (Yi et al. 2001), or the MIST evolutionary models

(Choi et al. 2016; Dotter 2016), which itself is built using MESA (Paxton et al. 2011, 2013, 2015, 2018). Stellar atmospheric models from NextGen (Allard et al. 2012), ATLAS (Kurucz 1979), and PHOENIX (Hauschildt et al. 1997) underlie several aspects of the code.

We are able to impose Gaussian priors on the stellar effective temperature ( $T_{\text{eff}}$ ) and metallicity ( $[\text{Fe}/\text{H}]$ ) in the fit, originating from the Keck/HIRES spectra (Table 2). The  $F_{\text{bol}}$  and  $T_{\text{eff}}$  parameters have enforced error floors representative of the systematic uncertainties between stellar evolution models to prevent unrealistic precision (2.0% and 2.4%, respectively; Tayar et al. 2022).

### 3.2. EXOFASTv2: RV Modeling

The multiple instrument RV data sets are simultaneously fit to a Keplerian model, retaining separate jitter and systemic offset terms. We measured typical  $\log R'_{\text{HK}}$  activity index measures of  $-5.1$  to  $-4.7$  that were uncorrelated with RV values. This activity level could induce stellar jitter up to  $\sim 10 \text{ m s}^{-1}$ , but is unlikely to affect the derived parameters given such a strong planetary signal.

Within EXOFASTv2 the exoplanet mass–radius relation from Chen & Kipping (2017) can be referenced to estimate the mass or radius of the exoplanet (and all relevant derived parameters) in the absence of an RV data set or transit, respectively. In this case, however, the RV data constrain the mass while the transit data constrain the radius.

A single long-term linear drift parameter is included in the model. We have excellent temporal overlap of the data across instruments, so there is no large correlation between the trend parameter and systemic RV offset parameters. The fitted RV model is shown in Figure 3.

### 3.3. EXOFASTv2: Transit Modeling

EXOFASTv2’s transit model is generated using Mandel & Agol (2002) and Agol et al. (2019) with limb-darkening parameters constrained by Claret & Bloemen (2011) and Claret (2017). We pass it the TESS coverage of the initial Sector 15–detected transit, a stretch of flat light curve from Sector 40 that narrowly missed another transit, as well as the later detection in Sector 56. We also include the entire 6 day NEOSSat light curve with its detection. Limb-darkening parameters and transit depths are allowed to differ between instruments. Each instrument also gets its own jitter parameter and out-of-transit offset value. We impose no additional transit-specific priors for this portion of the fit. The period and other orbital element constraints arise from a simultaneous fit of the transit and RV data.

We incorporate a spline fit in the EXOFASTv2 modeling of the NEOSSat data, based on the `keplerspline`<sup>51</sup> (Vanderburg et al. 2016) designed to handle long-term variability in long Kepler light curves. We used a knot spacing of 1.1 days (roughly  $3\times$  the transit duration) to model the low-frequency variation.

### 3.4. Bulk Planetary Composition

To infer the bulk composition of the planet, we use the modeling and retrieval approach of Thorngren & Fortney (2019), which we will briefly summarize. Forward models

<sup>51</sup> <https://github.com/avanderburg/keplerspline>

**Table 3**  
Median Values and 68% Confidence Intervals for TOI-2010

Parameter	Units	Values
Stellar Parameters:		
$M_*$	Mass ( $M_\odot$ )	$1.112^{+0.048}_{-0.055}$
$R_*$	Radius ( $R_\odot$ )	$1.079^{+0.027}_{-0.026}$
$R_{*,\text{SED}}$	Radius ( $R_\odot$ )	$1.0753^{+0.0093}_{-0.0090}$
$L_*$	Luminosity ( $L_\odot$ )	$1.299^{+0.083}_{-0.081}$
$F_{\text{Bol}}$	Bolometric flux (cgs)	$0.00000000354^{+0.00000000023}_{-0.00000000022}$
$\rho_*$	Density (cgs)	$1.243^{+0.087}_{-0.086}$
$\log g$	Surface gravity (cgs)	$4.417^{+0.021}_{-0.025}$
$T_{\text{eff}}$	Effective temperature (K)	$5929 \pm 74$
[Fe/H]	Metallicity (dex)	$0.168 \pm 0.055$
[Fe/H] <sub>0</sub>	Initial metallicity <sup>a</sup>	$0.154^{+0.054}_{-0.055}$
Age	Age (Gyr)	$1.9^{+2.2}_{-1.3}$
$A_V$	V-band extinction (mag)	$0.210^{+0.079}_{-0.085}$
$\sigma_{\text{SED}}$	SED photometry error scaling	$0.72^{+0.23}_{-0.15}$
$\varpi$	Parallax (mas)	$9.237 \pm 0.017$
$d$	Distance (pc)	$108.26 \pm 0.20$
$\dot{\gamma}$	RV slope <sup>b</sup> ( $\text{m s}^{-1} \text{ day}^{-1}$ )	$0.0185^{+0.0055}_{-0.0054}$
Planetary Parameters:		
		<b>b</b>
$P$	Period (days)	$141.834025^{+0.000065}_{-0.000066}$
$R_P$	Radius ( $R_J$ )	$1.054 \pm 0.027$
$M_P$	Mass ( $M_J$ )	$1.286^{+0.055}_{-0.057}$
$T_C$	Time of conjunction <sup>c</sup> (BJD <sub>TDB</sub> )	$2,458,712.30168^{+0.00042}_{-0.00041}$
$a$	Semimajor axis (au)	$0.5516^{+0.0078}_{-0.0093}$
$i$	Inclination <sup>d</sup> (degrees)	$89.903^{+0.064}_{-0.059}$
$e$	Eccentricity	$0.212^{+0.022}_{-0.021}$
$\omega_*$	Argument of periastron (degrees)	$98.8^{+4.8}_{-4.9}$
$T_{\text{eq}}$	Equilibrium temperature <sup>e</sup> (K)	$400.2^{+5.6}_{-5.7}$
$\tau_{\text{circ}}$	Tidal circularization timescale (Gyr)	$3,980,000^{+910,000}_{-790,000}$
$K$	RV semi-amplitude ( $\text{m s}^{-1}$ )	$47.8 \pm 1.5$
$R_P/R_*$	Radius of planet in stellar radii	$0.10035^{+0.00043}_{-0.00037}$
$a/R_*$	Semimajor axis in stellar radii	$109.8^{+2.5}_{-2.6}$
$\delta$	$(R_P/R_*)^2$	$0.010069^{+0.000087}_{-0.000075}$
$\delta_{\text{NEOSSat}}$	Transit depth in NEOSSat (fraction)	$0.01284^{+0.00040}_{-0.00038}$
$\delta_{\text{TESS}}$	Transit depth in TESS (fraction)	$0.01160 \pm 0.00011$
$\tau$	Ingress/egress transit duration (days)	$0.03363^{+0.0013}_{-0.00069}$
$T_{14}$	Total transit duration (days)	$0.3617^{+0.0012}_{-0.0010}$
$T_{\text{FWHM}}$	FWHM transit duration (days)	$0.32784^{+0.00083}_{-0.00082}$
$b$	Transit impact parameter	$0.147^{+0.088}_{-0.097}$
$b_S$	Eclipse impact parameter	$0.23^{+0.13}_{-0.15}$
$\tau_S$	Ingress/egress eclipse duration (days)	$0.0525^{+0.0035}_{-0.0028}$
$T_{S,14}$	Total eclipse duration (days)	$0.544^{+0.027}_{-0.025}$
$T_{S,\text{FWHM}}$	FWHM eclipse duration (days)	$0.491 \pm 0.025$
$\delta_{S,2.5 \mu\text{m}}$	Blackbody eclipse depth at $2.5 \mu\text{m}$ (ppm)	$0.0094^{+0.0020}_{-0.0017}$
$\delta_{S,5.0 \mu\text{m}}$	Blackbody eclipse depth at $5.0 \mu\text{m}$ (ppm)	$4.75^{+0.46}_{-0.43}$
$\delta_{S,7.5 \mu\text{m}}$	Blackbody eclipse depth at $7.5 \mu\text{m}$ (ppm)	$32.1^{+2.0}_{-1.9}$
$\rho_P$	Density (cgs)	$1.36^{+0.11}_{-0.10}$
$\log g_P$	Surface gravity	$3.457^{+0.024}_{-0.026}$
$\langle F \rangle$	Incident Flux ( $10^9 \text{ erg s}^{-1} \text{ cm}^{-2}$ )	$0.00557^{+0.00030}_{-0.00029}$
$T_P$	Time of periastron (BJD <sub>TDB</sub> )	$2,458,572.7 \pm 1.2$
$T_S$	Time of eclipse (BJD <sub>TDB</sub> )	$2,458,780.3^{+1.7}_{-1.6}$
$T_A$	Time of ascending node (BJD <sub>TDB</sub> )	$2,458,685.2 \pm 1.1$
$T_D$	Time of descending node (BJD <sub>TDB</sub> )	$2,458,595.5 \pm 1.1$
$e \cos \omega_*$		$-0.032 \pm 0.018$
$e \sin \omega_*$		$0.208^{+0.022}_{-0.021}$
$M_P \sin i$	Minimum mass ( $M_J$ )	$1.286^{+0.055}_{-0.057}$
$M_P/M_*$	Mass ratio	$0.001107^{+0.000039}_{-0.000038}$
$d/R_*$	Separation at midtransit	$86.8 \pm 4.2$
$P_T$	A priori nongrazing transit prob.	$0.01037^{+0.00053}_{-0.00048}$

**Table 3**  
(Continued)

Parameter	Units	Values		
$P_{T,G}$	A priori transit prob.	$0.01268^{+0.00065}_{-0.00059}$		
$P_S$	A priori nongrazing eclipse prob.	$0.006779^{+0.00010}_{-0.000068}$		
$P_{S,G}$	A priori eclipse prob.	$0.008291^{+0.00013}_{-0.000085}$		
Wavelength Parameters:		NEOSSat	TESS	
$u_1$	linear limb-darkening coeff.	$0.442 \pm 0.048$	$0.271 \pm 0.019$	
$u_2$	quadratic limb-darkening coeff.	$0.301 \pm 0.050$	$0.270 \pm 0.027$	
Telescope Parameters:		Levy	SOPHIE	Tull
$\gamma_{\text{rel}}$	Relative RV offset <sup>b</sup> (m s <sup>-1</sup> )	$0.3 \pm 1.3$	$-15,315.8^{+2.5}_{-2.4}$	$8778.8^{+2.9}_{-2.6}$
$\sigma_J$	RV jitter (m s <sup>-1</sup> )	$7.81^{+1.1}_{-0.97}$	$9.9^{+2.1}_{-1.7}$	$0.00^{+8.1}_{-0.00}$
$\sigma_J^2$	RV jitter variance	$60^{+18}_{-14}$	$97^{+46}_{-30}$	$-2^{+68}_{-39}$
Transit Parameters:				
TESS UT 2019-08-16				
$\sigma^2$	Added variance	$-0.000022669^{+0.000000031}_{-0.000000029}$		
$F_0$	Baseline flux	$1.000132^{+0.000030}_{-0.000031}$		
TESS UT 2021-07-23				
$\sigma^2$	Added variance	$-0.000000041^{+0.000000015}_{-0.000000014}$		
$F_0$	Baseline flux	$1.000002 \pm 0.000014$		
NEOSSat UT 2021-12-15				
$\sigma^2$	Added variance	$0.00001984^{+0.00000059}_{-0.00000057}$		
$F_0$	Baseline flux	$1.0003^{+0.0071}_{-0.0066}$		
TESS UT 2021-09-02				
$\sigma^2$	Added variance	$0.000000077^{+0.000000060}_{-0.000000058}$		
$F_0$	Baseline flux	$0.999961^{+0.000033}_{-0.000034}$		

**Notes.** See Table 3 in Eastman et al. (2019) for a detailed description of all parameters. Created Using EXOFASTv2 Commit Number 96030ceb.

<sup>a</sup> The metallicity of the star at birth.

<sup>b</sup> Reference epoch = 2,459,382.832843.

<sup>c</sup> Time of conjunction is commonly reported as the “transit time.”

<sup>d</sup> Inclination symmetrically on the other side of 90° is equally valid.

<sup>e</sup> Assumes no albedo and perfect redistribution. Calculated at a star–planet separation of  $a$ . See Table 4 for phase-specific values.

parameterize the thermal state of the planet by the envelope specific entropy, which we evolve from a hot initial state using the atmosphere models of Fortney et al. (2007). This requires that we know the radius and temperature structure of the planet at a given specific entropy. We calculate this using a 1D static model of the planet which solves the equations of hydrostatic equilibrium, conservation of mass, and the equation of state (EOS). We use the H/He EOS from Chabrier et al. (2019), and a 50/50 rock/ice mixture for the metals (Thompson 1990), combining these using the additive volumes approximation. For a given mass, metallicity, and stellar insolation, this yields evolution tracks of the radius with time. To match these models to TOI-2010 b, we use a Bayesian statistical model with the true mass, bulk metallicity, and true age as model parameters and fit them against the observed mass, radius, and age from the EXOFASTv2 fit (Table 3). Because TOI-2010 b is much cooler than the hot-Jupiter inflation threshold (e.g., Miller & Fortney 2011), we do not include any additional heating in the planet.

### 3.5. TESS Light-curve Modulation

Even in the PDCSAP TESS data, with a degree of its systematics removed, we noticed some low-level variability. As a secondary measure of stellar rotation we looked at the star’s long-term light-curve modulation. A simple normalization was

applied in order to concatenate the TESS 2 minute cadence SAP light curves from Sectors 14, 15, and 16. Data points that were flagged as poor quality, greater than  $5\sigma$  outliers, or during the TOI-2010 b transit were removed. Stitching together multiple sectors of observations (even when observed continuously) can introduce systematics into the concatenated light curve that could produce a spurious signal in a periodogram search. Therefore, we searched for periodic photometric variability using the TESS systematics-insensitive periodogram tool, TESS-SIP<sup>52</sup> (Hedges et al. 2020), which uses PCA to account for spacecraft systematics while simultaneously performing a periodogram search. In the periodogram search from 1 day to half the baseline of the continuous TESS observations (which are  $\sim 32$  days), we identify a periodic signature in the light curve at  $19.0 \pm 3.0$  days, albeit at a low normalized Lomb–Scargle power ( $< 0.001$ ). Assuming a small stellar obliquity, this 19 day signal corresponds to a  $\sim 2.8$  km s<sup>-1</sup> stellar rotation rate, in general agreement with the spectroscopic estimates (see Table 2). A short-period periodogram search (0.01–13 days) was also performed separately on the PDCSAP photometry from Sectors 14, 15, and 16 following the procedure described in Fetherolf et al. (2023). A small-amplitude ( $\lesssim 0.2$  ppt), 5.7 day signal was identified in the TESS photometry but we note this is consistent with being attributed to spacecraft

<sup>52</sup> <https://github.com/christinahedges/TESS-SIP>

systematics due to its location in power–period space relative to other stars in these TESS sectors. With its low S/N and similarity to known systematics, we do not consider this signal physically relevant.

### 3.6. WASP Light-curve Modulation

We searched each season of WASP data for a rotational modulation using methods discussed in Maxted et al. (2011). We find a significant and persistent modulation at a period of  $20 \pm 1$  days. The modulation is weak, with an amplitude of only 1–2 mmag, but the overall false-alarm likelihood is below 1%. This closely matches the TESS photometric modulation, and also likely reflects a stellar rotation rate of  $\sim 2.8 \text{ km s}^{-1}$ .

### 3.7. Mass–Orbit Possibilities for an Additional Companion

A small residual acceleration is detected in the collective RV data. To constrain potential objects on very long orbits that could cause this acceleration, we adopt the process described in Bryan et al. (2016). In essence, we step through a 2D grid of semimajor axes and object masses. In each cell, we draw a set of planet b parameters from our fitted posteriors of Table 3, generating an RV model. This model is subtracted from the RV measurements to reveal a residual slope. A model for object 2 is created by drawing  $M$  and  $a$  values from the current cell, and  $i$  and  $e$  values from motivated distributions. In this case,  $i$  is drawn randomly from a uniform  $\cos i$  distribution and  $e$  from a  $\beta$  distribution (Equation (3) of Bryan et al. 2016). The remaining  $T_0$ ,  $T_{\text{peri}}$ , and  $\omega$  parameters are determined by fitting the drawn object 2 model to the residuals, as well as an RV offset. The offset accounts for any change to the assumed systemic velocity caused by the second object.

This process is repeated 500 times per cell. For each cycle, the  $\chi^2$  is calculated and stored, as well as the probability that the object is visible. This probability is based on the inferred magnitude of the object and the fraction of its orbital period that it would spend at a detectable separation from the host, set by the Gemini-N/‘Alopec contrast curve (Figure 2). The data cubes are marginalized over the third axis to create a 2D probability density grid over the object’s  $a$  and  $M$ . These results are displayed in Figure 5.

With the allowable mass–orbit space mapped out, we investigate the potential for the known nearby stars to cause the acceleration. The plotted mass uncertainties for the two nearby sources in Figure 5 reflect the magnitude uncertainty of the source only. They do not account for the intrinsic uncertainty of the precalculated stellar evolution grids<sup>53</sup> (Baraffe et al. 2015) from which they were interpolated.

To place a tentative uncertainty on the semimajor axis of the neighboring stars (under the assumption they are bound), we follow the steps of Brandeker et al. (2006, Appendix A2) given an observed projected separation, unknown orbital orientation, and assumed eccentricity distribution. We do not adopt their analytic approximation (Equation (A2)) which roughly matches the numerical distribution arising from a simple  $f(e) = e^2$  eccentricity distribution, but instead carry out the full Monte Carlo approach to create a nonanalytic distribution. We use  $f(e) = e^{0.4}$  where  $e \in [0, 0.8]$  is extracted from the observation of binaries with Sun-like primaries (Moe & Di Stefano 2017).

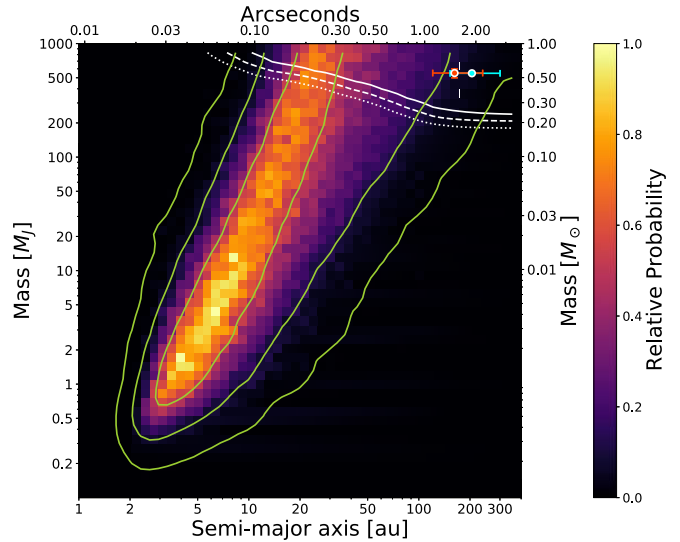


**Figure 5.** Constraints on a potential second bound body in the system creating the observed long-term RV acceleration, assuming the objects are at the same distance as TOI-2010. Small-orbit limits are provided by the long baseline over which the gradual acceleration occurs. Green contours show the 0.607, 0.135, and 0.011 relative probability levels, corresponding to the 1, 2, and 3 $\sigma$  probability density values of a normal distribution. White contours show the 25%, 50%, and 75% detection probability levels (from bottom to top) set by the Gemini-N/‘Alopec contrast curve. Contours are smoothed by a Gaussian kernel with a standard deviation of one cell. Red and cyan points in the top right corner indicate the ‘Alopec-discovered (1''5) and Gaia (1''9) close neighbor stars.

## 4. Results

Based on the results of the global transit, RV, and SED fit, we confirm TOI-2010 b as a temperate Jovian exoplanet around a Sun-like star. We find TOI-2010 b to have a mass of  $M_P = 1.286^{+0.055}_{-0.057} M_J$  and a radius of  $R_P = 1.054 \pm 0.027 R_J$ . It orbits with a period of  $P = 141.834025^{+0.000065}_{-0.000066}$  days and an eccentricity of  $e = 0.212^{+0.022}_{-0.021}$ . A full list of the fitted and calculated parameters and their uncertainties are displayed in Table 3. We determine that the contribution to the uncertainty of  $M_P$  is almost evenly split between the uncertainties on  $K$  and  $M_*$ , and that the uncertainties of  $i$ ,  $e$ , and  $P$  have a negligible impact.

The reported  $T_{\text{eq}}$  of Table 3 comes from an assessment using a single representative star–planet distance. However, with nonnegligible eccentricity, several calculated parameters,  $T_{\text{eq}}$  included, are subject to variation with orbital phase. Table 4 displays a certain of these parameters at four key points in the planet’s orbit.

TOI-2010 b’s moderate eccentricity falls in the  $\sim 75$ th percentile of giant planets with well-known masses and radii. It is distinctly above the cluster of planets with very low eccentricities, but not so high as to stand out among the population of high-eccentricity planets.

Between the SED/MIST model fitting within EXOFASTv2 and the spectral analysis from various instruments, we determine many of TOI-2010’s stellar parameters. In the global EXOFASTv2 posteriors, we see no sign of the bimodality commonly seen between stellar mass and age. This can arise when a star is slightly evolved and the MIST stellar evolution models experience some degeneracy near the subgiant branch (e.g., Dalba et al. 2021).

From the Keck/HIRES spectral measurement, we find the stellar radius, mass, and effective temperature to be

<sup>53</sup> <http://perso.ens-lyon.fr/isabelle.baraffe/BHAC15dir/>



**Table 4**  
Orbital Information

Parameter	Periastron	Apastron	Transit	Eclipse	Units
Phase	0.016	0.516	0.000	0.479	...
Orbital distance	0.44	0.70	0.44	0.67	au
Insolation	6.9	2.9	6.8	2.9	$S_{\odot}$
$T_{\text{eq}}$	450	363	450	364	K

**Note.** The  $T_{\text{eq}}$  calculation assumes no albedo and perfect redistribution.

$R_{\star} = 1.084^{+0.028}_{-0.027} R_{\odot}$ ,  $M_{\star} = 1.107^{+0.050}_{-0.057} M_{\odot}$ , and  $T_{\text{eff}} = 5917 \pm 75$  K, respectively. TOI-2010 has a surface gravity of  $\log g = 4.412^{+0.023}_{-0.026}$  and a metallicity of  $[\text{Fe}/\text{H}] = 0.169^{+0.055}_{-0.056}$ . We used these Keck/HIRES stellar values in the global fit as this spectral measurement has the highest resolution and S/N. The stellar parameters determined via spectral fitting of the Keck/HIRES, LCOGT/NRES, and FLWO/TRES data sets (Table 2) show close agreement in general. However, the instruments report distinct values for the stellar rotation ( $v \sin i_{\star}$ ), though all indicate a slowly rotating star ( $< 5 \text{ km s}^{-1}$ ). The discrepancies between the instruments may be due to differences in spectral resolution and S/N, or potentially the slow rotation of the star itself. For slowly rotating stars, the effects of rotationally induced line broadening can be of similar magnitude to other broadening mechanisms (e.g., thermal, pressure, and turbulence). Disentangling them becomes challenging, and thus  $v \sin i_{\star}$  may be inflated if some mechanisms are not properly considered. We therefore report the spectrally derived rotation rates as rough upper limits (Table 2).

We note that the photometric modulations seen in the TESS and WASP light curves both suggest an equatorial rotation of  $\sim 2.8 \text{ km s}^{-1}$ , falling in the middle of the spectral  $v \sin i_{\star}$  values. The precise value is not central to any key findings of our study, but it does have some bearing on estimates of a potential RM signal for future endeavors. We adopt the modulation-derived value for RM calculations in Section 5.2 as it bypasses the line-broadening issues of a slow rotator.

Available data on the local stellar environment reveals two faint neighbors to TOI-2010. We use `tpfplotter`<sup>54</sup> (Aller et al. 2020) to visualize the TESS aperture and Gaia positional information jointly (Figure 6). The only Gaia star of note within the TESS aperture is 5 mag fainter and separated from TOI-2010 by  $1''.9$  at a position angle of  $33^{\circ}$  east of north (Gaia ID: 2136815881247621760). The PDCSAP flux used in our light-curve analysis accounts for this minor dilution so as not to affect the radius estimate of the planet.

Though absent from the Gaia catalog, we photometrically detect a second neighbor in the immediate vicinity of TOI-2010 using ‘Alopec high-contrast imaging. It is of similar brightness to the Gaia star ( $\Delta \text{mag} = 5 \pm 0.5$ ) and was detected at a separation of  $1''.5$ ,  $138^{\circ}$  east of north. The flux dilution from the ‘Alopec star is small enough to cause  $< 1\%$  deviation in the  $R_p/R_{\star}$  measurement.

Spectral investigation for evidence of blended binaries also shows no indication of significant contamination. In the SOPHIE spectra, the corresponding bisectors of the cross-correlation functions do not show any significant variation nor correlation with the RV. This means there are no indications for RV variations induced by blend configurations or stellar

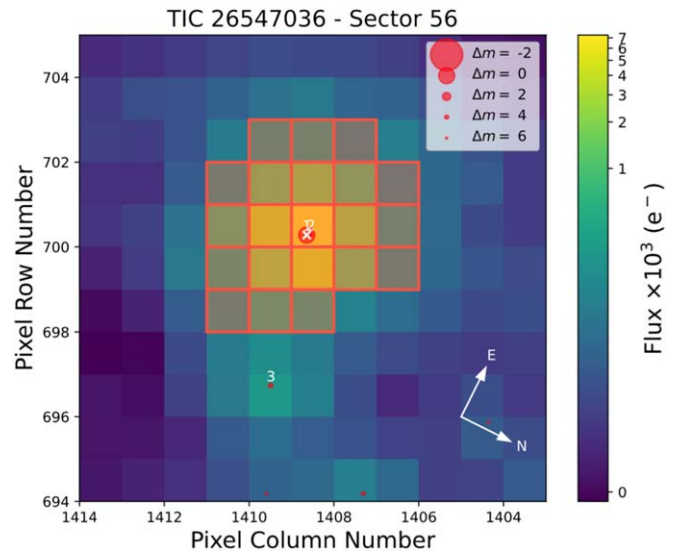


**Figure 6.** Visual comparison of TESS photometry and nearby Gaia stars. Only one notable Gaia star contaminates the aperture (labeled “2”) with a separation of  $1''.9$  and fainter by  $\Delta m \sim 5$ . The TESS PDCSAP flux values account for this very minor dilution.

activity. We also computed cross-correlations using masks characteristic of different spectral types: all produce similar RV variations, suggesting against the presence of a blend of stars with different spectral types. Similarly, the Keck template spectrum was run through the `ReaMatch` (Kolbl et al. 2015) software to check for blended stellar spectra. The analysis revealed no hint of any such blended components in its cross-correlation routines, and limits any unresolved sources to well below 1% of TOI-2010’s flux.

With the lack of any photometric or spectroscopic evidence for significant or problematic nearby or blended stars, we conclude that the measurements of TOI-2010 are free of any significant stellar contamination. The planet radius assessment of TOI-2010 b is therefore robust.

The bulk metallicity results are shown in Figure 7. The bulk metal mass fraction of  $Z_p = 0.11$  corresponds to 45 Earth masses of heavy elements. There appears to be a small degeneracy between age and metallicity in this analysis. This arises because leftover heat from formation in a young star ( $< 1$  Gyr) is compensated in the model with extra metal.

In this case we used a fully mixed planet model. Using a “core+envelope” model would mean replacing compressible gas in the core with less compressible metals, requiring more metals to achieve the same radius. This model would require  $\sim 20\%$  (or  $\sim 1\sigma$ ) extra, according to Thorngren et al. (2016). The result is similar when using a moderate number of layers making up a semiconvective staircase “core,” but when considering thousands of layers (e.g., Leconte & Chabrier 2012) cooling slows down and even more metal is required. However, simulations suggest that small layers merge quickly as the planet evolves (Moll et al. 2017; Vazan et al. 2018), so we would not assume such an extreme case without more evidence.

The RV fit reveals a residual acceleration of  $\dot{\gamma} = 0.0185 \pm 0.0055 \text{ m s}^{-1} \text{ day}^{-1}$ . This  $\sim 3\sigma$  slope detection is suggestive of some additional distant planetary or stellar companion acting on the system. In running the RV data through a generalized Lomb–Scargle periodogram (Lomb 1976; Scargle 1982; Zechmeister & Kürster 2009) within the `astropy` package

<sup>54</sup> <https://github.com/jlillo/tpfplotter>

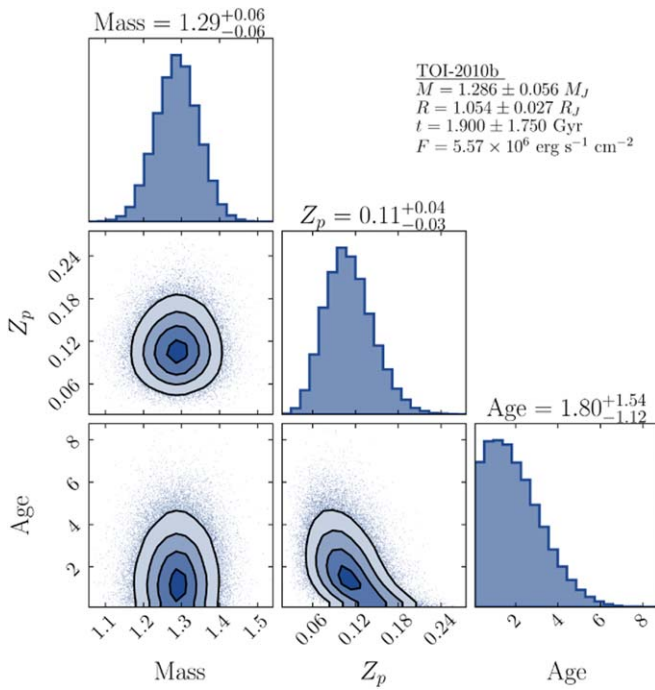


**Figure 7.** Results of the planet’s bulk metallicity analysis. Here mass is reported in Jupiter units,  $Z_p$  is the bulk metal mass fraction of the planet, and the age is given in gigayears. The small inset table shows the input priors used.

(Astropy Collaboration et al. 2013, 2018, 2022), the obvious 142 day signal stands out with indisputable significance. Removing the best-fit Keplerian RV model of planet b (Figure 3) and rerunning the periodogram on the residuals produces no peaks with false-alarm probabilities better than  $\sim 10\%$ . These findings are shown in Figure 8. There appear to be no other periodic signals present in our data set for  $P \lesssim 1000$  days.

We also check the TESS light curves for additional transits. Using the `astropy.stats.BoxLeastSquares` (BLS) function, we scan the available photometry for periodic transit-like signals. With two known TOI-2010 b transits in the data, the procedure flags the 1134 day separation along with accompanying aliases (including the 142 day true period). Removing the two known transits leaves a very flat light curve, and a second BLS pass detects nothing above the noise level. The BLS algorithm is sensitive only to repeated events, and so single transits (e.g., due to very long periods or transits falling in the observing gaps) would not be detected here. A visual inspection of the light curve reveals no obvious transits to indicate additional bodies in the system.

To explore the possible very-long-period scenarios, we employed a 2D grid search of semimajor axis and companion mass combinations that might produce the observed RV acceleration (Bryan et al. 2016). The resulting relative probability map marks correlated boundaries on the probable configurations (Figure 5). At the low-mass end, the system could harbor an object of  $0.4 M_J$  orbiting at 2.6 au. Anything interior and/or less massive than that struggles to match the observed acceleration. For sources remaining below the photometric detection threshold, the most probable configuration at the high-mass end is a  $475 M_J$  ( $0.46 M_\odot$ ) object orbiting at  $\sim 22$  au, however the allowable configuration space becomes quite broad. As we are now in the range of self-luminous low-mass main-sequence stars, the Gemini-N/‘Alopeke speckle

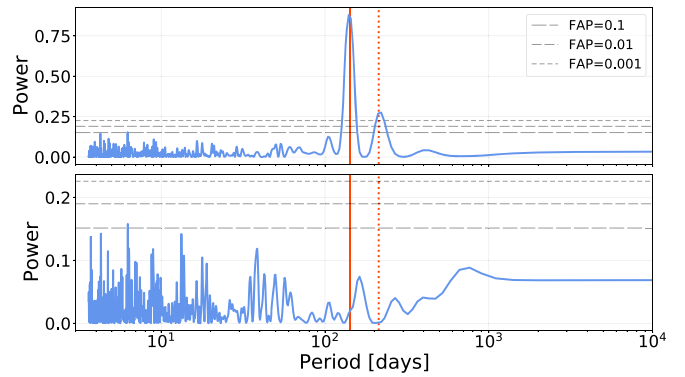


**Figure 8.** Lomb–Scargle periodogram of RV data. False-alarm probabilities (FAPs) are shown in gray. The red solid line indicates the fitted period of TOI-2010 b, and the dotted red line is the 3/2 harmonic. The top panel periodogram shows results of the unaltered data set, whereas data used for the bottom panel has had the 141.8 day signal removed. With the removal of planet b’s signal, no other significant power remains at any searchable period.

imaging would likely detect anything more massive or more separated (i.e., above the white contours).

In determining the plausibility of each close neighbor star causing the RV acceleration, we estimate some of their relevant properties. We determine the  $1''5$  ‘Alopeke star to have a mass of  $M = 0.525^{+0.045}_{-0.049} M_\odot$  and a semimajor axis of  $a = 162.16^{+75.33}_{-41.43}$  au, while the  $1''9$  Gaia star has  $M = 0.5226^{+0.0001}_{-0.0001} M_\odot$  and  $a = 205.21^{+95.33}_{-52.43}$  au. These estimates, though rough, allow us to place both stars on the Figure 5 grid.

If neither of these nearby stars are the cause, the most likely candidate is a yet-unseen planetary or low-mass stellar object along the high-probability region in Figure 5. This region through the explored parameter space roughly follows the trend of  $M/[M_J] \approx 0.015(a/[au])^{3.2}$  where  $a > 3$  au.

## 5. Discussion

### 5.1. TOI-2010 b in Context

With physical and orbital parameters of the TOI-2010 b system properly constrained, we can place it in the context of other known exoplanets. Using planet data gathered using `ExoFile`<sup>55</sup> from the NASA Exoplanet Archive (2023), Figure 9 shows several properties for the population of confirmed giant planets ( $R > 0.5 R_J$ ). As can be seen in the top panel, TOI-2010 b is deep in the low-insolation wings of the population. Few other confirmed giants can boast such low stellar input, and fewer still have magnitudes bright enough to enable detailed spectroscopic follow up. TOI-2010 b stands out as valuable addition to this corner of parameter space.

The bottom panel of Figure 9 locates TOI-2010 b in mass and radius space. A distinction is made between strongly and weakly irradiated planets (dotted line in the top panel and marker type in the bottom panel), given that their mass–radius relationship changes. We find TOI-2010 b to be a fairly typically proportioned giant planet, akin to Jupiter though quite a bit warmer. Its moderate eccentricity may suggest a dynamic history either in its formation or due to ongoing interaction with unseen neighbors.

<sup>55</sup> <https://github.com/AntoineDarveau/exofile>

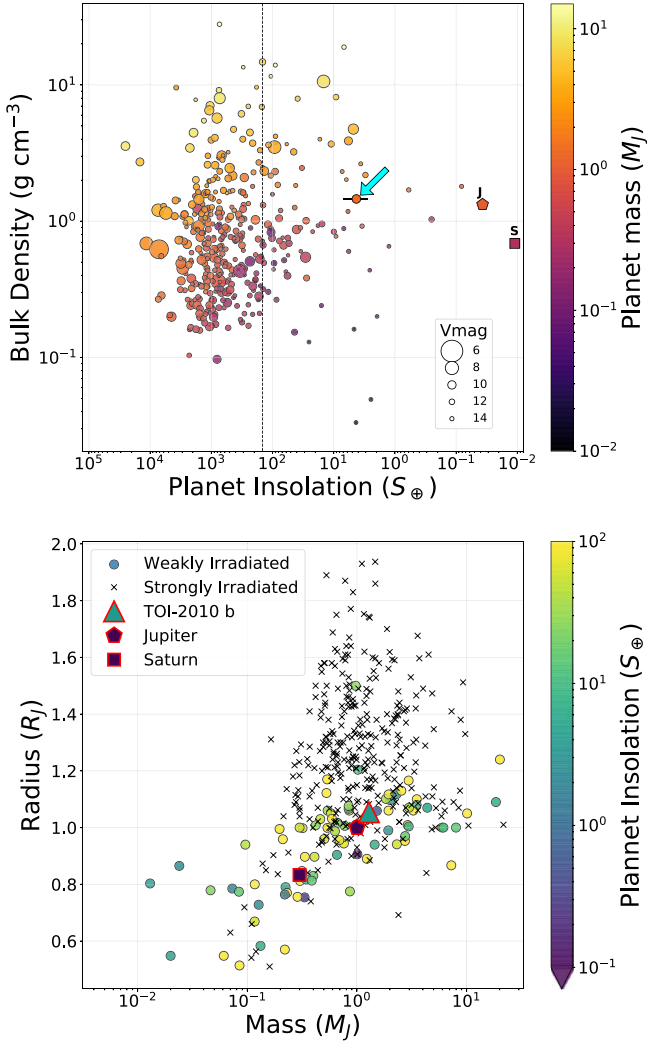


**Figure 9.** Population of confirmed giant ( $R > 0.5 R_J$ ) transiting planets with available insolation values and better than 50% uncertainties on mass and radius. Top: the dotted vertical line indicates the empirical inflation boundary (Demory & Seager 2011; Miller & Fortney 2011) where planet radii are seen to increase with insolation. TOI-2010 b is indicated with the cyan arrow, and Jupiter and Saturn are labeled toward the right. Bottom: the same population of giant planets separated into strongly and weakly irradiated subgroups according to the boundary in the above plot.

### 5.2. Future Observation Potential

We determine the expected signal strengths for a number of potential observations that might be made on this target in the future (Figure 10). We calculate and report the Kempton et al. (2018) Transmission Spectroscopy Metric (TSM), though we note it was calibrated for smaller planets. The TSM nominally provides an S/N estimate for fixed-duration observations made with JWST/NIRISS. However, without the small-planet-calibrated scaling factor, the specific values of Figure 10(a) may be better interpreted by their relative strengths, rather than absolute value. We use TOI-2010 b’s transit-phase equilibrium temperature (450 K) for this calculation, and in doing so we find that it has moderate transmission spectroscopy potential with  $TSM \sim 26$ . As a relative measure, it lands at the  $\sim 23$ rd percentile for the population plotted in Figures 9 and 10.

We can also look at the Emission Spectroscopy Metric (ESM) of Kempton et al. (2018). Similarly to the TSM, the ESM estimates the S/N achieved with a mid-infrared

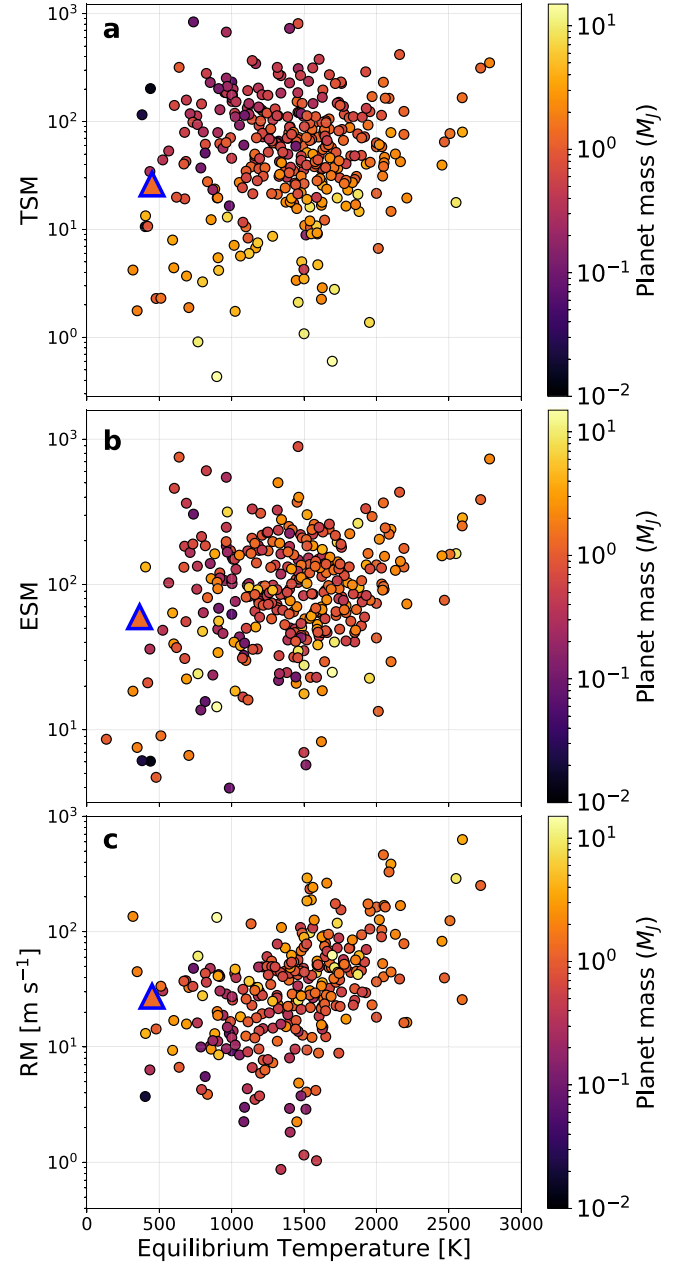


**Figure 10.** Comparison of expected signal strengths for the same planet population shown in Figure 9. TOI-2010 b is indicated with the triangle marker. Panel (a): TSM. The TSM provides an S/N estimate for a JWST/NIRISS transit observation. Panel (b): ESM. The ESM provides an S/N estimate for a JWST/MIRI eclipse observation. Panel (c): RM signal amplitude. The TOI-2010 b value in this plot uses  $v \sin i_* = 2.8 \text{ km s}^{-1}$ , derived from the TESS and WASP light-curve modulations.

secondary eclipse detection by JWST. We find a more promising scenario in emission than with transmission. Using the eclipse-phase equilibrium temperature (364 K), TOI-2010 b has one of the strongest predicted emission signals ( $ESM \sim 60$ ) among cool giants  $\lesssim 750 \text{ K}$ . Even against giant planets as a whole, TOI-2010 b falls near the median value. The ESM does not include an empirical calibration like the TSM, and so the values indicate the expected S/N of a JWST secondary eclipse detection with the MIRI instrument. TOI-2010 b may provide a very interesting test bed for certain atmospheric properties. The  $T_{eq}$  range of 360–450 K across its orbit spans a transition regime where disequilibrium chemistry may be evident.



**Table 5**  
Median Values and 68% Confidence Interval for Transit Times and Depths

Transit	Planet	Epoch	$T_T$	Depth
TESS UT 2019-08-16	b	0	$2,458,712.30168^{+0.00042}_{-0.00041}$	$0.011598 \pm 0.000052$
NEOSSat UT 2021-12-11	b	6	$2,459,563.30584^{+0.00028}_{-0.00027}$	$0.01246 \pm 0.00026$
TESS UT 2022-09-02	b	8	$2,459,846.97389 \pm 0.00034$	$0.011598 \pm 0.000052$

Models by Fortney et al. (2020) predict this temperature range to exhibit marked changes in CO/CH<sub>4</sub> and N<sub>2</sub>/NH<sub>3</sub> ratios between equilibrium and disequilibrium conditions. Such detections may go a long way toward connecting models across the Jupiter–exoplanet–brown dwarf continuum.

We also compute the potential for making an obliquity measurement using the RM effect. Winn (2010, Equation (40)) provides an approximation for calculating the  $\Delta RV$  amplitude expected during transit for given planet/star size ratio, impact parameter, and projected equatorial velocity ( $v \sin i_*$ ) of the star. Adopting  $v \sin i_* = 2.8 \text{ km s}^{-1}$ , derived from the modulations observed in both the TESS and WASP light curves, we calculate an RM amplitude of  $27.5 \text{ m s}^{-1}$  (Figure 10(c)).

### 5.3. Single-transit Planets

Any transit survey mission is eventually bound to produce single-transit targets. It comes as a direct consequence of having only a finite monitoring time for a particular star, and the potential for exoplanets to have very long orbits. With TESS’s month-long baseline coverage for most of the sky, single-transit targets are not infrequent. Passively detected retransits in subsequent sectors can help narrow down options, but long gaps between detections leave many possible period aliases. The survey’s schedule of reobserving a target is also not always compatible with the planet’s orbit. For example, the second detected transit of TOI-2010 b in Sector 56 was very nearly missed. If the period had turned out even 0.6% longer ( $\sim 19 \text{ hr}$ ), the additional TESS transit would have been missed entirely.

Without substantial active follow-up effort, single-transit planets often remain unviable for further study. Any phase/timing-related endeavors cannot be scheduled without a firm ephemeris, and attempting an RV study of the system requires careful vetting even before investing the sizeable observing program for the RVs themselves. Happily, the TFOP has a wide variety of researchers, infrastructure, and resources to put toward the effort. If a candidate proves suitable for RV follow up (as was the case for TOI-2010), the mass measurement and orbital refinement come packaged together. This provides a lot of value for the RV investment. That being said, RV-derived periods generally have uncertainties on the scale of hours or days for single-transit targets (which tend to have longer orbits), and the predictive timing uncertainty on future transits only grows worse as transits go undetected. This ephemeris is generally insufficiently refined to plan precisely timed observations (e.g., transits and eclipses), but it does open the door for the last step needed to constrain the system neatly.

The  $3\sigma$  uncertainty window of an RV-predicted transit can easily span up to 20 days or more. Photometric instruments that are able to locate a transit within such a wide window can refine the period uncertainties to the order of minutes. The space-based vantage point provided by NEOSSat and other small space telescopes (e.g., CHEOPS; Benz et al. 2021) is ideal for this application. Such facilities can monitor this star

over the whole time frame, and their detections do not even have to be of particularly high S/N. The single high-quality TESS measurement is generally sufficient to constrain the transit shape, and so a low S/N additional transit can simply supply timing information beyond the precision of the RVs. Being able to point at a target at any time also allows space-faring instruments to narrow down possible period aliases quickly if two widely spaced transits have been detected.

It is a major and ongoing challenge to carry out successful retransit searches for TESS single-transit targets. The nature of the mission’s sector-by-sector and hemisphere-by-hemisphere observing strategy leaves plenty of room for longer-period planets to fall through the cracks. Small space telescopes are uniquely suited in providing support observations to pull these long-period planets back from the edge of obscurity by firmly establishing their ephemerides. Table 5 lists the constrained transit timings of TOI-2010b, uniquely determining the period and enabling the scheduling of future observations.

### 5.4. Cause of the RV Acceleration

We believe that the  $1''.9$  Gaia neighbor is unlikely to be the cause of the residual RV slope for two reasons. First, the Gaia DR3 parallax distances of TOI-2010 and this faint neighbor differ by 1.5 pc. This does place the source as a close neighbor in interstellar terms, but given their respective parallax uncertainties their distances are more than  $2\sigma$  discrepant. It is therefore very likely to be physically separated from TOI-2010 at the parsec scale and thus could not cause the observed acceleration given its low magnitude-inferred mass. Second, even if we assume some bias on the parallax measure and that they are indeed at the same distance as one another, this companion does not fall in a favorable location of the Figure 5 plot. The source’s inferred mass and orbital separation place it away from the high-probability region. The specific relative probability of its location is only  $\sim 5\%$  of the global peak probability, and  $\sim 7\%$  of the highest-probability region at its particular mass. The combination of these two reasons disfavor the Gaia star as the source of the acceleration.

The  $1''.5$  source found in the ‘Alopeke image may be a slightly better candidate, though it is missing some crucial information. With a similar inferred mass but tighter separation, this source is closer to the high-likelihood region of the Figure 5 plot. Its particular cell is  $\sim 12\%$  of the peak probability for this mass. The uncertainty on its semimajor axis allows for it to intersect a bit deeper into the high-probability region. However, with an unknown parallax, it is entirely possible that this is a background or foreground object and wholly unassociated with the system.

Based on their low-probability locations in the search grid, coupled with a parsec-scale difference in distance between the Gaia neighbor and TOI-2010 and lack of parallax information on the ‘Alopeke neighbor, it appears unlikely that either star is responsible for the RV acceleration.



The presence of these two sources certainly does not rule out the additional possibility of a hidden lower-mass object. The ‘Alopeke source may be approaching the right region of parameter space, but the unknown nature of its 3D location relative to TOI-2010 precludes any certainty for now. Further characterization of the nearby sources may offer more clarity, such as refinement of the Gaia star’s parallax, or a check on the ‘Alopeke star’s proper motion in a few years time. Additional RV coverage of TOI-2010 may even reveal some clear curvature to the residual acceleration, which would add strong constraints on the high-mass/wide-orbit end of the currently allowed parameter space.

## 6. Summary

In the course of this study, we have confirmed the planetary nature of the exoplanet TOI-2010 b. A wide range of data sets from the TESS mission and the TFOP working group were collected in this effort. Most notably, the initial single transit discovered in the TESS Sector 15 data provided strong transit morphology constraints, but no information on the period. A substantial RV campaign involving several observatories mapped the RV curve, determined a rough period, and predicted a subsequent transit to an uncertainty of a few days. Using NEOSat, we observed a continuous week-long window and caught this transit, refining the period down to just a few minutes uncertainty. A fortuitous catch in TESS’s Sector 56 light curve revealed an additional transit detection at a late stage of this manuscript’s preparation.

We carried out a global model fit using EXOFASTv2 to determine the system’s physical and orbital parameters by simultaneously fitting time-series light curves, RVs, and historical photometric data. TOI-2010 b turns out to be Jupiter-like in size, about 30% more massive, and its equilibrium temperature may fluctuate between roughly 360–450 K given its moderately eccentric orbit.

Our bulk metallicity analysis also suggests a fairly Jupiter-like metal mass fraction, i.e., modestly lower than the general trend given its mass (Thorngren et al. 2016). The host star is very slightly super-solar in terms of mass, radius, luminosity, and temperature.

We find evidence of a small-amplitude residual acceleration in the RV data set once TOI-2010 b’s signal has been removed, potentially indicative of an outer companion in the system. Searching a broad grid of potential mass and semimajor axis values, we determine the relative probability that such companions could cause the observed acceleration. We also determine which of these simulated systems would be visible in our high-contrast imaging. Among hidden objects (too faint and/or close to TOI-2010 to be detected), we find a correlated allowed parameter space ranging 0.4–475  $M_J$  in mass ( $475 M_J \approx 0.45 M_\odot$ ) and 2.6–23 au in semimajor axis along its highest-probability region. Smaller masses and orbits cannot reproduce the observed RV slope, while more massive (i.e., brighter) objects on wider orbits would be observable in our Gemini-N/‘Alopeke speckle imaging.

We make note of two nearby sources that could potentially be connected to the acceleration. A Gaia source, 1.9 away, is at a similar distance to the TOI-2010 system, but perhaps not close enough to be considered a binary capable of producing the RV slope. Also, its inferred mass and semimajor axis do not fall in a likely region of the parameter space. A second source, discovered in our high-contrast imaging 1.5 away, has an

inferred mass and semimajor axis that are slightly more likely to produce the acceleration. However, with no parallax information, this source could easily be just a projected neighbor.

In refining TOI-2010 b’s period, we have enabled future transit/eclipse-based research. In large part due to its cool temperature, the transmission spectroscopy potential of this target is somewhat poor. However, its predicted signal strength is much better for emission spectroscopy and RM measurements.

TOI-2010 b turns out to be very typical member of the population of known Jovian exoplanets. However, the planet’s unique value and interest stem from its observability and low insolation/effective temperature. Currently, among giant planets with reliable radius and mass measurements, only  $\sim 20$  are at comparable or lower stellar insolation levels. Among those, only two are bright targets.

TOI-2010 b is a successful case of searching for and catching additional transits for a single-transit candidate planet. This process is often expensive and challenging, but it allows us to build up the confirmed exoplanet catalog where it is only sparsely populated.

## Acknowledgments

C.R.M. and D.L. acknowledge funding from the Trottier Family Foundation in their support of Trottier Institute for Research on Exoplanets (iREx). They also acknowledge individual funding from the Natural Sciences and Engineering Research Council (NSERC) of Canada. P.A.D. acknowledges support by a 51 Pegasi b Postdoctoral Fellowship from the Heising-Simons Foundation and by a National Science Foundation (NSF) Astronomy and Astrophysics Postdoctoral Fellowship under award AST-1903811.

S.D. is funded by the UK Science and Technology Facilities Council (grant No. ST/V004735/1).

X.D. and T.Fo. acknowledge funding from the French National Research Agency in the framework of the Investissements d’Avenir program (ANR-15-IDEX-02), through the funding of the “Origin of Life” project of the Grenoble-Alpes University.

E.M. acknowledges funding from FAPEMIG under project number APQ-02493-22 and research productivity grant No. 309829/2022-4 awarded by the CNPq, Brazil.

D.D. acknowledges support from the NASA Exoplanet Research Program grant 18-2XRP18\_2-0136, and from the TESS Guest Investigator Program grants 80NSSC22K1353 and 80NSSC22K0185.

T.Fe. acknowledges support from the University of California President’s Postdoctoral Fellowship Program.

K.A.C. and D.W.L. acknowledge support from the TESS mission via subaward s3449 from MIT.

The authors would like to thank the on-duty telescope observers Patrick Newman, Owen Alfaro, Ben Chang, and William McLaughlin for their contribution in gathering the George Mason University Observatory data.

This paper made use of data collected by the TESS mission and are publicly available from the Mikulski Archive for Space Telescopes (MAST) operated by the Space Telescope Science Institute (STScI). Funding for the TESS mission is provided by NASA’s Science Mission Directorate.

We acknowledge the use of public TESS data from pipelines at the TESS Science Office and at the TESS Science Processing Operations Center.

Resources supporting this work were provided by the NASA High-End Computing (HEC) Program through the NASA Advanced Supercomputing (NAS) Division at Ames Research Center for the production of the SPOC data products.

We would like to thank the PIs of the TESS Guest Investigator programs that put TOI-2010 on the 2 minute (Steven Villanueva—G04195, Diana Dragomir—G04231, Andrej Prsa—G04171, Andrew Mayo—G04242, and James Davenport—G04039) and 20 s (Guadalupe Tovar Mendoza—G05121, and Daniel Huber—G05144) cadence lists.

This research has made use of the Exoplanet Follow-up Observation Program (ExoFOP; doi:10.26134/ExoFOP5) website, which is operated by the California Institute of Technology, under contract with the National Aeronautics and Space Administration under the Exoplanet Exploration Program.

We would like to thank and acknowledge the efforts of the TESS Single Transit Planet Candidate working group for working to keep tabs on and improving our understanding of long-period targets.

This work makes use of observations from the LCOGT network. Part of the LCOGT telescope time was granted by NOIRLab through the Mid-Scale Innovations Program (MSIP). MSIP is funded by the NSF.

Observations in the paper (Program ID: GN-2021A-LP-105) made use of the high-resolution imaging instrument ‘Alopec’. ‘Alopec’ was funded by the NASA Exoplanet Exploration Program and built at the NASA Ames Research Center by Steve B. Howell, Nic Scott, Elliott P. Horch, and Emmett Quigley. ‘Alopec’ was mounted on the Gemini-North telescope of the international Gemini Observatory, a program of NSF’s NOIRLab, which is managed by the Association of Universities for Research in Astronomy (AURA) under a cooperative agreement with the National Science Foundation on behalf of the Gemini Observatory partnership: the National Science Foundation (United States), National Research Council (Canada), Agencia Nacional de Investigación y Desarrollo (Chile), Ministerio de Ciencia, Tecnología e Innovación (Argentina), Ministério da Ciência, Tecnologia, Inovações e Comunicações (Brazil), and Korea Astronomy and Space Science Institute (Republic of Korea).

This work is based on observations collected with the SOPHIE spectrograph on the 1.93 m telescope at the Observatoire de Haute-Provence (CNRS), France. We thank the staff of the Observatoire de Haute-Provence for their support at the 1.93 m telescope and on SOPHIE. We also thankfully acknowledge grants from CNES and the CNRS “Programme National de Planétologie.”

This research has made use of the NASA Exoplanet Archive, which is operated by the California Institute of Technology, under contract with the National Aeronautics and Space Administration under the Exoplanet Exploration Program.

This work has made use of data from the European Space Agency Gaia (<https://www.cosmos.esa.int/gaia>), processed Data Processing and Analysis Consortium (DPAC; <https://www.cosmos.esa.int/web/gaia/dpac/consortium>). Funding for the DPAC has been provided by national institutions, in particular the institutions participating in the Gaia Multilateral Agreement.

*Software:* lightkurve (Lightkurve Collaboration et al. 2018), EXOFASTv2 (Eastman et al. 2019), ReaMatch (Kolbl et al. 2015), astropy (Astropy Collaboration et al.

2013, 2018, 2022), matplotlib (Hunter 2007), Numpy (van der Walt et al. 2011; Harris et al. 2020), tpfplotter,<sup>57</sup> ExoFile,<sup>58</sup> KeplerSpline (Vanderburg et al. 2016), TESS-SIP (Hedges et al. 2020), SpeckMatch (Petigura 2015; Petigura et al. 2017; Yee et al. 2017), Astro-ImageJ (Collins et al. 2017), alnitak,<sup>59</sup> AUSTRAL (Endl et al. 2000), BANZAI-NRES (McCully et al. 2022), and PyAstronomy<sup>60</sup> (Czesla et al. 2019).

## Appendix

Here in Table 6 we present the RV measurements that were used in our global fit. The RV data used in the global fit are displayed in Table 6. The data span three instruments and include their individual RV offsets.

**Table 6**  
RV Measurements of TOI-2010

BJD <sub>TDB</sub>	RV (m s <sup>-1</sup> )	$\sigma_{RV}$ (m s <sup>-1</sup> )	Inst.
2,458,887.037868	-65.7	8.1	Levy
2,458,895.027687	-71.6	6.5	Levy
2,458,899.012701	-35.9	5.6	Levy
2,458,922.023014	-8.4	6.4	Levy
2,458,955.028682	39.1	4.4	Levy
2,458,961.908021	41.6	6.6	Levy
2,458,964.893612	48.0	5.0	Levy
2,458,966.898471	31.0	9.0	Levy
2,458,970.887634	38.8	6.5	Levy
2,458,973.892349	47.6	5.1	Levy
2,458,991.906717	10.7	8.9	Levy
2,459,030.819021	-42.9	5.4	Levy
2,459,040.997378	-22.5	4.5	Levy
2,459,064.767218	-6.9	4.7	Levy
2,459,068.806213	-0.4	4.4	Levy
2,459,182.597717	-38.5	5.6	Levy
2,459,185.604636	-26.5	5.0	Levy
2,459,188.603420	-34.3	4.6	Levy
2,459,194.590484	-25.0	6.9	Levy
2,459,203.597023	-12.1	5.9	Levy
2,459,222.590712	0.7	5.9	Levy
2,459,225.067097	46.2	8.8	Levy
2,459,228.601064	30.8	7.6	Levy
2,459,235.060004	25.8	6.1	Levy
2,459,262.996513	45.1	9.2	Levy
2,459,274.930264	22.9	6.7	Levy
2,459,287.907247	-33.7	6.3	Levy
2,459,295.883380	-40.4	6.7	Levy
2,459,301.842307	-47.0	6.3	Levy
2,459,307.004259	-55.4	4.3	Levy
2,459,315.878742	-28.7	4.7	Levy
2,459,319.949170	-36.2	4.0	Levy
2,459,322.978069	-34.2	4.4	Levy
2,459,326.986152	-33.7	5.4	Levy
2,459,333.953995	-27.9	4.7	Levy
2,459,336.970295	-14.1	5.7	Levy
2,459,339.999687	-20.1	4.5	Levy
2,459,344.872338	9.5	5.1	Levy
2,459,347.947959	0.7	4.3	Levy
2,459,351.983896	-3.0	5.6	Levy
2,459,356.940402	19.2	4.8	Levy
2,459,361.893688	22.2	4.4	Levy
2,459,364.922348	23.0	4.9	Levy
2,459,368.925800	9.8	5.0	Levy
2,459,372.940835	46.4	7.7	Levy

<sup>57</sup> <https://github.com/jlillo/tpfplotter>

<sup>58</sup> <https://github.com/AntoineDarveau/exofile>

<sup>59</sup> <https://github.com/oalfaro2/alnitak>

<sup>60</sup> <https://github.com/sczesla/PyAstronomy>

**Table 6**  
(Continued)

BJD <sub>TDB</sub>	RV (m s <sup>-1</sup> )	$\sigma_{RV}$ (m s <sup>-1</sup> )	Inst.
2,459,381.765521	26.3	5.5	Levy
2,459,385.822790	45.6	4.4	Levy
2,459,388.885495	46.5	6.5	Levy
2,459,392.788945	35.9	5.0	Levy
2,459,395.795554	51.9	4.3	Levy
2,459,398.811073	60.4	4.5	Levy
2,459,401.841438	37.1	4.6	Levy
2,459,404.841232	40.2	4.8	Levy
2,459,407.851764	23.1	4.1	Levy
2,459,409.840484	26.1	4.3	Levy
2,459,410.773285	24.0	4.4	Levy
2,459,412.737338	28.5	4.4	Levy
2,459,415.750915	16.4	4.8	Levy
2,459,419.751557	-11.5	4.6	Levy
2,459,424.700659	-8.0	5.0	Levy
2,459,427.744671	-19.6	4.7	Levy
2,459,434.772695	-23.3	4.4	Levy
2,459,438.778047	-59.5	4.6	Levy
2,459,452.747840	-47.4	4.5	Levy
2,459,464.768780	-32.5	5.1	Levy
2,459,464.768780	-32.5	5.1	Levy
2,459,489.826089	-9.1	4.8	Levy
2,459,522.781338	44.9	6.1	Levy
2,459,586.597180	-35.6	5.6	Levy
2,459,607.020932	-38.8	6.4	Levy
2,459,039.4716	-15,360.0	3.0	SOPHIE
2,459,113.4148	-15,277.0	3.0	SOPHIE
2,459,133.4087	-15,305.0	6.0	SOPHIE
2,459,394.5368	-15,278.0	4.0	SOPHIE
2,459,419.5450	-15,304.0	5.0	SOPHIE
2,459,445.4901	-15,378.0	3.0	SOPHIE
2,459,469.4911	-15,340.0	3.0	SOPHIE
2,459,477.4045	-15,323.0	7.0	SOPHIE
2,459,483.4480	-15,324.0	5.0	SOPHIE
2,459,501.3575	-15,312.0	3.0	SOPHIE
2,459,548.2221	-15,276.0	5.0	SOPHIE
2,459,553.2376	-15,298.0	4.0	SOPHIE
2,459,559.2231	-15,299.0	3.0	SOPHIE
2,459,567.2305	-15,330.0	3.0	SOPHIE
2,459,571.2387	-15,348.0	3.0	SOPHIE
2,459,631.7057	-15,312.0	3.0	SOPHIE
2,459,662.6759	-15,259.0	4.0	SOPHIE
2,459,731.5828	-15,359.0	3.0	SOPHIE
2,459,750.5120	-15,352.0	3.0	SOPHIE
2,459,773.5751	-15,290.0	3.0	SOPHIE
2,459,786.6144	-15,290.0	4.0	SOPHIE
2,459,805.5426	-15,267.0	9.0	SOPHIE
2,459,811.3339	-15,241.0	4.0	SOPHIE
2,459,828.3791	-15,264.0	3.0	SOPHIE
2,459,191.579631	8750.7	12.1	Tull
2,459,192.588106	8747.0	10.8	Tull
2,459,275.950854	8817.7	13.3	Tull
2,459,276.970138	8798.1	10.6	Tull
2,459,277.969833	8777.6	10.0	Tull
2,459,293.930022	8740.0	10.4	Tull
2,459,294.957330	8737.9	11.5	Tull
2,459,301.941670	8729.9	13.7	Tull
2,459,339.884675	8763.0	11.0	Tull
2,459,340.824938	8757.6	10.4	Tull
2,459,355.874441	8794.3	11.6	Tull
2,459,383.844963	8823.0	11.2	Tull
2,459,384.820734	8811.8	10.0	Tull
2,459,411.737865	8795.2	9.6	Tull
2,459,413.773637	8798.0	9.0	Tull
2,459,878.627818	8753.2	11.6	Tull

**ORCID iDs**

Christopher R. Mann  <https://orcid.org/0000-0002-9312-0073>  
 Paul A. Dalba  <https://orcid.org/0000-0002-4297-5506>

David Lafrenière  <https://orcid.org/0000-0002-6780-4252>  
 Benjamin J. Fulton  <https://orcid.org/0000-0003-3504-5316>  
 Xavier Delfosse  <https://orcid.org/0000-0001-5099-7978>  
 Thierry Forveille  <https://orcid.org/0000-0003-0536-4607>  
 Eder Martioli  <https://orcid.org/0000-0002-5084-168X>  
 Claire Moutou  <https://orcid.org/0000-0002-2842-3924>  
 Michael Endl  <https://orcid.org/0000-0002-7714-6310>  
 William D. Cochran  <https://orcid.org/0000-0001-9662-3496>  
 Franck Marchis  <https://orcid.org/0000-0001-7016-7277>  
 Diana Dragomir  <https://orcid.org/0000-0003-2313-467X>  
 Arvind F. Gupta  <https://orcid.org/0000-0002-5463-9980>  
 Dax L. Feliz  <https://orcid.org/0000-0002-2457-7889>  
 Belinda A. Nicholson  <https://orcid.org/0000-0003-1360-4404>  
 Steven Villanueva, Jr.  <https://orcid.org/0000-0001-6213-8804>  
 Jason Rowe  <https://orcid.org/0000-0002-5904-1865>  
 Geert Jan Talens  <https://orcid.org/0000-0003-4787-2335>  
 Daniel Thorngren  <https://orcid.org/0000-0002-5113-8558>  
 Daryll LaCourse  <https://orcid.org/0000-0002-8527-2114>  
 Tom Jacobs  <https://orcid.org/0000-0003-3988-3245>  
 Andrew W. Howard  <https://orcid.org/0000-0001-8638-0320>  
 Allyson Bieryla  <https://orcid.org/0000-0001-6637-5401>  
 David W. Latham  <https://orcid.org/0000-0001-9911-7388>  
 Markus Rabus  <https://orcid.org/0000-0003-2935-7196>  
 Tara Fetherolf  <https://orcid.org/0000-0002-3551-279X>  
 Coel Hellier  <https://orcid.org/0000-0002-3439-1439>  
 Steve B. Howell  <https://orcid.org/0000-0002-2532-2853>  
 Peter Plavchan  <https://orcid.org/0000-0002-8864-1667>  
 Michael Reefer  <https://orcid.org/0000-0003-4701-8497>  
 Justin Wittrock  <https://orcid.org/0000-0002-7424-9891>  
 George R. Ricker  <https://orcid.org/0000-0003-2058-6662>  
 S. Seager  <https://orcid.org/0000-0002-6892-6948>  
 Joshua N. Winn  <https://orcid.org/0000-0002-4265-047X>  
 Jon M. Jenkins  <https://orcid.org/0000-0002-4715-9460>  
 Thomas Barclay  <https://orcid.org/0000-0001-7139-2724>  
 David Watanabe  <https://orcid.org/0000-0002-3555-8464>  
 Karen A. Collins  <https://orcid.org/0000-0001-6588-9574>  
 Jason D. Eastman  <https://orcid.org/0000-0003-3773-5142>  
 Eric B. Ting  <https://orcid.org/0000-0002-8219-9505>

**References**

- Abbasi, V., Thorsteinson, S., Balam, D., et al. 2019, in 1st NEO and Debris Detection Conference, 22, ed. T. Flohrer, R. Jehn, & F. Schmitz (Paris: ESA)
- Agol, E., Luger, R., & Foreman-Mackey, D., 2019 [rodluger/Limbdark.jl](https://arxiv.org/abs/1907.08761), Zenodo, doi:10.5281/zenodo.3515456
- Allard, F., Homeier, D., & Freytag, B. 2012, *RSPTA*, 370, 2765
- Aller, A., Lillo-Box, J., Jones, D., Miranda, L. F., & Barceló Forteza, S. 2020, *A&A*, 635, A128
- Astropy Collaboration, Price-Whelan, A. M., Lim, P. L., et al. 2022, *AJ*, 935, 167
- Astropy Collaboration, Price-Whelan, A. M., Sipőcz, B. M., et al. 2018, *AJ*, 156, 123
- Astropy Collaboration, Robitaille, T. P., Tollerud, E. J., et al. 2013, *A&A*, 558, A33
- Baraffe, I., Homeier, D., Allard, F., & Chabrier, G. 2015, *A&A*, 577, A42
- Baruteau, C., Crida, A., Paardekooper, S. J., et al. 2014, in Protostars and Planets VI, ed. H. Beuther et al. (Tucson, AZ: Univ. Arizona Press), 667
- Beatty, T. G., & Gaudi, B. S. 2008, *ApJ*, 686, 1302
- Benz, W., Broeg, C., Fortier, A., et al. 2021, *ExA*, 51, 109
- Bianchi, L., Herald, J., Efremova, B., et al. 2011, *Ap&SS*, 335, 161
- Bouchy, F., Díaz, R. F., Hébrard, G., et al. 2013, *A&A*, 549, A49
- Bouchy, F., Hébrard, G., Udry, S., et al. 2009, *A&A*, 505, 853



- Brandeker, A., Jayawardhana, R., Khavari, P., Haisch, K. E., Jr., & Mardones, D. 2006, *ApJ*, **652**, 1572
- Brown, T. M., Baliber, N., Bianco, F. B., et al. 2013, *PASP*, **125**, 1031
- Bryan, M. L., Knutson, H. A., Howard, A. W., et al. 2016, *ApJ*, **821**, 89
- Buchhave, L. A., Bizzarro, M., Latham, D. W., et al. 2014, *Natur*, **509**, 593
- Buchhave, L. A., Bakos, G. Á., Hartman, J. D., et al. 2010, *ApJ*, **720**, 1118
- Buchhave, L. A., Latham, D., Johansen, A., et al. 2012, *Natur*, **486**, 375
- Burt, J., Holden, B., Hanson, R., et al. 2015, *JATIS*, **1**, 044003
- Butler, R. P., Marcy, G. W., Williams, E., et al. 1996, *PASP*, **108**, 500
- Chabrier, G., Mazevet, S., & Soubiran, F. 2019, *ApJ*, **872**, 51
- Chen, J., & Kipping, D. 2017, *ApJ*, **834**, 17
- Choi, J., Dotter, A., Conroy, C., et al. 2016, *ApJ*, **823**, 102
- Claret, A. 2017, *A&A*, **600**, A30
- Claret, A., & Bloemen, S. 2011, *A&A*, **529**, A75
- Collins, K. A., Kielkopf, J. F., Stassun, K. G., & Hessman, F. V. 2017, *AJ*, **153**, 77
- Cooke, B. F., Pollacco, D., Anderson, D. R., et al. 2021, *MNRAS*, **500**, 5088
- Cutri, R. M., Skrutskie, M. F., van Dyk, S., et al. 2003, *yCat*, II/246
- Cutri, R. M., Wright, E. L., Conrow, T., et al. 2021, *yCat*, II/328
- Czesla, S., Schröter, S., Schneider, C. P., et al. 2019 *PyA: Python Astronomy-related Packages*, Astrophysics Source Code Library, ascl:1906.010
- Dalba, P. A., Kane, S. R., Dragomir, D., et al. 2022, *AJ*, **163**, 61
- Dalba, P. A., Kane, S. R., Li, Z., et al. 2021, *AJ*, **162**, 154
- Demory, B.-O., & Seager, S. 2011, *ApJS*, **197**, 12
- Dong, C., Lingam, M., Ma, Y., & Cohen, O. 2017, *ApJL*, **837**, L26
- Dotter, A. 2016, *ApJS*, **222**, 8
- Eastman, J. D., Rodriguez, J. E., Agol, E., et al. 2019, arXiv:1907.09480
- Endl, M., Kürster, M., & Els, S. 2000, *A&A*, **362**, 585
- Fetherolf, T., Pepper, J., Simpson, E., et al. 2023, *ApJS*, **268**, 22
- Fűrész, G. 2008, PhD thesis, University of Szeged, Hungary
- Fortney, J. J., Marley, M. S., & Barnes, J. W. 2007, *ApJ*, **659**, 1661
- Fortney, J. J., Visscher, C., Marley, M. S., et al. 2020, *AJ*, **160**, 288
- Fox, C., & Wiegert, P. 2022, *MNRAS*, **516**, 4684
- Fulton, B. J., Weiss, L. M., Sinukoff, E., et al. 2015, *ApJ*, **805**, 175
- Gaia Collaboration 2020, *yCat*, I/350
- Gaia Collaboration, Brown, A. G. A., Vallenari, A., et al. 2018, *A&A*, **616**, A1
- Gaia Collaboration, Prusti, T., de Bruijne, J. H. J., et al. 2016, *A&A*, **595**, A1, J. H. J.
- Gao, P., Wakeford, H. R., Moran, S. E., & Parmentier, V. 2021, *JGRE*, **126**, e06655
- Goldreich, P., & Tremaine, S. 1980, *ApJ*, **241**, 425
- Greiss, S., Steeghs, D., Gänsicke, B. T., et al. 2012, *AJ*, **144**, 24
- Harris, C. R., Millman, K. J., van der Walt, S. J., et al. 2020, *Natur*, **585**, 357
- Hauschildt, P. H., Baron, E., & Allard, F. 1997, *ApJ*, **483**, 390
- Hébrard, G., Bouchy, F., Pont, F., et al. 2008, *A&A*, **488**, 763
- Hedges, C., Angus, R., Barentsen, G., et al. 2020, *RNAAS*, **4**, 220
- Henden, A. A., Templeton, M., Terrell, D., et al. 2016, *yCat*, II/336
- Høg, E., Fabricius, C., Makarov, V. V., et al. 2000, *A&A*, **355**, L27
- Hörst, S. M., He, C., Lewis, N. K., et al. 2018, *NatAs*, **2**, 303
- Howell, S. B., Everett, M. E., Sherry, W., Horch, E., & Ciardi, D. R. 2011, *AJ*, **142**, 19
- Howell, S. B., Scott, N. J., Matson, R. A., et al. 2021, *FrASS*, **8**, 10
- Hunter, J. D. 2007, *CSE*, **9**, 90
- Jenkins, J. M. 2002, *ApJ*, **575**, 493
- Jenkins, J. M., Chandrasekaran, H., McCauliff, S. D., et al. 2010, *Proc. SPIE*, **7740**, 77400D
- Jenkins, J. M., Tenenbaum, P., Seader, S., et al. 2020, *Kepler Data Processing Handbook: Transiting Planet Search*, Kepler Science Document KSCI-19081-003 003, NASA Ames Research Center
- Jenkins, J. M., Twicken, J. D., McCauliff, S., et al. 2016, *Proc. SPIE*, **9913**, 99133E
- Kempton, E. M. R., Bean, J. L., Louie, D. R., et al. 2018, *PASP*, **130**, 114401
- Kolb, R., Marcy, G. W., Isaacson, H., & Howard, A. W. 2015, *AJ*, **149**, 18
- Kristiansen, M. H. K., Rappaport, S. A., Vanderburg, A. M., et al. 2022, *PASP*, **134**, 074401
- Kurucz, R. L. 1979, *ApJS*, **40**, 1
- Kurucz, R. L. 1992, in *IAU Symp. 149, The Stellar Populations of Galaxies*, ed. B. Barbuy & A. Renzini (Dordrecht: Kluwer), 225
- Landsman, W. B. 1993, in *ASP Conf. Ser. 52, Astronomical Data Analysis Software and Systems II*, ed. R. J. Hanisch, R. J. V. Brissenden, & J. Barnes (San Francisco, CA: ASP), 246
- Leconte, J., & Chabrier, G. 2012, *A&A*, **540**, A20
- Lightkurve Collaboration, Cardoso, J. V. D. M., Hedges, C., et al., 2018 *Lightkurve: Kepler and TESS Time Series Analysis in Python*, Astrophysics Source Code Library, ascl:1812.013
- Lin, D. N. C., & Papaloizou, J. 1986, *ApJ*, **309**, 846
- Lomb, N. R. 1976, *Ap&SS*, **39**, 447
- Mandel, K., & Agol, E. 2002, *ApJL*, **580**, L171
- Maxted, P. F. L., Anderson, D. R., Collier Cameron, A., et al. 2011, *PASP*, **123**, 547
- McCully, C., Daily, M., Brandt, G. M., et al., 2022 *BANZAI-NRES: BANZAI Data Reduction Pipeline for NRES*, Astrophysics Source Code Library, ascl:2212.012
- Mermilliod, J. C. 1994, *yCat*, II/193
- Miller, N., & Fortney, J. J. 2011, *ApJL*, **736**, L29
- Moe, M., & Di Stefano, R. 2017, *ApJS*, **230**, 15
- Moll, R., Garaud, P., Mankovich, C., & Fortney, J. J. 2017, *ApJ*, **849**, 24
- Mordasini, C. 2020, *A&A*, **638**, A52
- Nagasawa, M., Ida, S., & Bessho, T. 2008, *ApJ*, **678**, 498
- NASA Exoplanet Archive 2023, *Planetary Systems*, v2023-01-20 16:08, NExSci-Caltech/IPAC, doi:10.26133/NEA12
- Niemann, H. B., Atreya, S. K., Carignan, G. R., et al. 1998, *JGR*, **103**, 22831
- Owen, J. E., & Wu, Y. 2013, *ApJ*, **775**, 105
- Paunzen, E. 2015, *A&A*, **580**, A23
- Paxton, B., Bildsten, L., Dotter, A., et al. 2011, *ApJS*, **192**, 3
- Paxton, B., Cantiello, M., Arras, P., et al. 2013, *ApJS*, **208**, 4
- Paxton, B., Marchant, P., Schwab, J., et al. 2015, *ApJS*, **220**, 15
- Paxton, B., Schwab, J., Bauer, E. B., et al. 2018, *ApJS*, **234**, 34
- Perruchot, S., Kohler, D., Bouchy, F., et al. 2008, *Proc. SPIE*, **7014**, 70140J
- Petigura, E. A. 2015, PhD thesis, University of California, Berkeley
- Petigura, E. A., Howard, A. W., Marcy, G. W., et al. 2017, *AJ*, **154**, 107
- Pollacco, D., Skillen, I., Collier Cameron, A., et al. 2008, *MNRAS*, **385**, 1576
- Pollacco, D. L., Skillen, I., Collier Cameron, A., et al. 2006, *PASP*, **118**, 1407
- Radovan, M. V., Cabak, G. F., Laiterman, L. H., Lockwood, C. T., & Vogt, S. S. 2010, *Proc. SPIE*, **7735**, 77354K
- Rasio, F. A., & Ford, E. B. 1996, *Sci*, **274**, 954
- Ricker, G. R., Winn, J. N., Vanderspek, R., et al. 2015, *JATIS*, **1**, 014003
- Savitzky, A., & Golay, M. J. E. 1964, *AnaCh*, **36**, 1627
- Scargle, J. D. 1982, *ApJ*, **263**, 835
- Schlaflly, E. F., & Finkbeiner, D. P. 2011, *ApJ*, **737**, 103
- Schlegel, D. J., Finkbeiner, D. P., & Davis, M. 1998, *ApJ*, **500**, 525
- Siverd, R. J., Brown, T. M., Barnes, S., et al. 2018, *Proc. SPIE*, **10702**, 107026C
- Smith, J. C., Stumpe, M. C., Van Cleve, J. E., et al. 2012, *PASP*, **124**, 1000
- Stumpe, M. C., Smith, J. C., Catanzarite, J. H., et al. 2014, *PASP*, **126**, 100
- Stumpe, M. C., Smith, J. C., Van Cleve, J. E., et al. 2012, *PASP*, **124**, 985
- Tayar, J., Claytor, Z. R., Huber, D., & van Saders, J. 2022, *ApJ*, **927**, 31
- Thompson, S. L. 1990, *ANEOS Analytic Equations of State for Shock Physics Codes Input Manual* SAND-89-2951 ON: DE90010198, Sandia National Lab
- Thorngren, D., & Fortney, J. J. 2019, *ApJL*, **874**, L31
- Thorngren, D., Gao, P., & Fortney, J. J. 2019, *ApJL*, **884**, L6
- Thorngren, D. P., Fortney, J. J., Murray-Clay, R. A., & Lopez, E. D. 2016, *ApJ*, **831**, 64
- Tody, D. 1986, *Proc. SPIE*, **627**, 733
- Tody, D. 1993, in *ASP Conf. Ser. 52, Astronomical Data Analysis Software and Systems II*, ed. R. J. Hanisch, R. J. V. Brissenden, & J. Barnes (San Francisco, CA: ASP), 173
- Torres, G., Andersen, J., & Giménez, A. 2010, *A&ARv*, **18**, 67
- Tull, R. G., MacQueen, P. J., Sneden, C., & Lambert, D. L. 1995, *PASP*, **107**, 251
- Twicken, J. D., Catanzarite, J. H., Clarke, B. D., et al. 2018, *PASP*, **130**, 064502
- van der Walt, S., Colbert, S. C., & Varoquaux, G. 2011, *CSE*, **13**, 22
- Vanderburg, A., Latham, D. W., Buchhave, L. A., et al. 2016, *ApJS*, **222**, 14
- Vazan, A., Helled, R., & Guillot, T. 2018, *A&A*, **610**, L14
- Vogt, S. S., Allen, S. L., Bigelow, B. C., et al. 1994, *Proc. SPIE*, **2198**, 362
- Ward, W. R. 1997, *Icar*, **126**, 261
- Winn, J. N. 2010, arXiv:1001.2010
- Wu, Y., & Lithwick, Y. 2011, *ApJ*, **735**, 109
- Wu, Y., & Murray, N. 2003, *ApJ*, **589**, 605
- Yee, S. W., Petigura, E. A., & von Braun, K. 2017, *ApJ*, **836**, 77
- Yi, S., Demarque, P., Kim, Y.-C., et al. 2001, *ApJS*, **136**, 417
- Zacharias, N., Finch, C. T., Girard, T. M., et al. 2012, *yCat*, I/322A
- Zechmeister, M., & Kürster, M. 2009, *A&A*, **496**, 577